

CMB signature of non-thermal Dark Matter produced from self-interacting dark sector

Dilip Kumar Ghosh,^{1,*} Purusottam Ghosh,^{1,†} and Sk Jeusun^{1,‡}

¹*School of Physical Sciences, Indian Association for the Cultivation of Science,
2A & 2B Raja S.C. Mullick Road, Kolkata 700032, India*

Abstract

The basic idea of this work is to achieve the observed relic density of a non-thermal dark matter(DM) and its connection with Cosmic Microwave Background (CMB) via additional relativistic degrees of freedom which are simultaneously generated during the period T_{BBN} to T_{CMB} from a long-lived dark sector particle. To realize this phenomena we minimally extend the type-I seesaw scenario with a Dirac fermion singlet(χ) and a complex scalar singlet (φ) which transform non-trivially under an unbroken symmetry \mathcal{Z}_3 . χ being the lightest particle in the dark sector acts as a stable dark matter candidate while the next to lightest state φ operates like a long lived dark scalar particle. The initial density of φ can be thermally produced through either self-interacting number changing processes ($3\varphi \rightarrow 2\varphi$) within dark sector or the standard annihilation to SM particles ($2\varphi \rightarrow 2 \text{ SM}$). The late time (after neutrino decoupling) non-thermal decay of φ can produce dark matter in association with active neutrinos. The presence of extra relativistic neutrino degrees of freedom at the time of CMB can have a significant impact on ΔN_{eff} . Thus the precise measurement of ΔN_{eff} by current PLANCK 2018 collaboration and future experiments like SPT-3G and CMB-S4 can indirectly probe this non-thermal dark matter scenario which is otherwise completely secluded due to its tiny coupling with the standard model.

*Electronic address: tpdkg@iacs.res.in

†Electronic address: spspg2655@iacs.res.in

‡Electronic address: skjeesun48@gmail.com

I. INTRODUCTION

The standard model (SM) of particle physics has been extraordinarily victorious in explaining properties of elementary particles of the universe and their interactions through strong, electromagnetic and weak forces. The SM seems complete after the discovery of Higgs-like particle with mass $M_h = 125$ GeV at the Large Hadron Collider (LHC)[1, 2], which is responsible for mass generation mechanism through electroweak symmetry breaking in the SM. In spite of the great triumph of the SM, several theoretical and experimental issues still persist, that demands physics beyond the framework of the Standard Model. Based on numerous astrophysical and cosmological observations at a wide range of length scales, it is now well established fact that about 80% of total mass of the universe consists of Dark matter (DM)[3–6] with relic density ($\Omega_{\text{DM}}h^2 = 0.120 \pm 0.001$) [6]. Another astonishing experimental evidence is the observation of tiny but non-zero neutrino masses ($m_\nu \lesssim \mathcal{O}(10^{-10})$ GeV) and neutrino flavour oscillations [7–12]. To address these issues, various theoretical as well as phenomenological ideas have been proposed. The issue of neutrino masses and their mixing angles can be resolved by the Seesaw mechanisms [13–22]. However, any direct experimental verification of these ideas are yet to be confirmed. While in the dark matter sector, weakly interacting massive particles (WIMP) [23–28] is the most popular and widely studied thermal DM candidate whose interaction strength with SM particles is of the order of electroweak interactions and via freeze-out mechanism it fits nicely the observed relic density of the universe. Nevertheless, null measurements from various dark matter detection experiments [29–41] severely restricts the WIMP freeze-out mechanism and forcing us to think if the standard WIMP paradigm is just waning or it is already deceased. To bypass this deadlock, an alternative framework, coined as *freeze-in* mechanism has been proposed. In this framework DM is a feebly interacting massive particle (FIMP) whose interactions with SM plasma is too small $\lesssim \mathcal{O}(10^{-10})$ to keep them in thermal bath [42–47]. Rather FIMPs are produced non-thermally either from decay or annihilation of bath particles in the early universe. The FIMP freezes in once the temperature of the universe becomes lower than the FIMP mass and produces DM relic abundance in the correct ballpark as observed today. Moreover, FIMPs having such a petite coupling with SM particles can easily accommodate various non-observational signature of DM in different detection experiments like Panda [29], XENON [30], LUX [31]. However, some attempts have been

made to test the FIMP scenario in direct search experiments [48, 49], and indirectly using observational data from big bang nucleosynthesis (BBN) or cosmic microwave background (CMB) [50–56]. Furthermore, non-thermal production of DM from the decay of heavier dark sector particles have also been studied in literature [57–60].

Apart from FIMP, strongly interacting massive particle(SIMP) is another alternate paradigm to explain the DM abundance [61–63] as well as the structure formation of the universe[64–66]. SIMPs are produced thermally in the early universe by number changing processes within itself. SIMP scenario requires strong self interaction and very small annihilation rate to SM particles contrary to WIMPs to successfully satisfy the correct DM relic density [67–69].

On the other hand Cosmic Microwave Background (CMB) is an ideal probe of the physics in the early universe. The very precise measurement of anisotropies in the temperature of photons which dissociate from visible sector in the recombination phase of the thermal evolution of our universe, leads to the determination of the energy density in that particular era. From this one can estimate the number of light species in the universe and in the massless limit this is provided by the relativistic degrees of freedom g_* [70, 71]. On the other hand after neutrino decoupling, one recasts the number of light degrees of freedom associated with neutrino bath as N_{eff} and in the SM it is roughly number of active neutrinos ($N_\nu = 3$). Thus any physics scenarios beyond the SM (BSM) with new light degrees of freedom with masses \mathcal{O} (eV) or less can subscribe to N_{eff} . We have very precise information of N_{eff} from recent Planck 2018 [6], which suggests N_{eff} at the time of CMB formation to be $N_{\text{eff}}^{\text{CMB}} = 2.99_{-0.33}^{+0.34}$ at 95% confidence level (C.L), whereas in the SM, $N_{\text{eff}}^{\text{SM}} = 3.045$. The quantity N_{eff} is parameterized as $N_{\text{eff}} \equiv (\rho_{\text{rad}} - \rho_\gamma)/\rho_\nu$, where, ρ_γ , ρ_ν , and ρ_{rad} denote the photon energy density, active neutrino energy density and total radiation energy density of the universe respectively [72]. The deviation from 3, the number of active neutrinos can be attributed to various non-trivial effects like non-instantaneous neutrino decoupling, finite temperature QED corrections to the electromagnetic plasma, flavour oscillations of neutrinos [72–75]. Multiple upcoming experiments like SPT-3G[76], CMB-S4[77] are going to be extremely sensitive to the presence of any new radiation /light degrees of freedom and will put stringent bound on $\Delta N_{\text{eff}} = N_{\text{eff}} - N_{\text{eff}}^{\text{SM}} \approx 0.06$ at 95% confidence level. There also exists strong constraint on the changes in N_{eff} between BBN and CMB epoch as explored by ref.[78]. Various BSM scenarios that entail additional entropy injection to the neutrino sector

can face a tough challenge from the measurement of ΔN_{eff} by both the present and future generation CMB experiments [79–84]. This precise measurement of ΔN_{eff} has also non-trivial implications on various new physics models that produce dark matter in associated with the injection of additional light degrees of freedom [85–88]. Recently, studies with ΔN_{eff} have been explored in the context of resolving the discrepancy between local measurement and CMB estimation of the Hubble constant (H_0) [89, 90].

In this work, we are interested in non thermal production of dark matter from heavier dark sector, where the dark sector may or may not have sizeable interaction with the SM bath. To realize this picture we extend the SM by one complex SM gauge singlet scalar (φ), one gauge singlet Dirac fermion (χ) and 3 right handed neutrinos (RHN)($N_{1,2,3}$). The three RHNs are responsible for neutrino mass generation through well known Type-I seesaw mechanism[14, 91]. φ and χ are dark sector particles and an additional discrete \mathcal{Z}_3 symmetry has been imposed under which they transform non trivially while the rest of the particles transform trivially. In our analysis lightest dark sector particle χ can play the role of DM whereas the heavy dark sector particle (φ) is a long lived owing to its very small coupling ($\lesssim 10^{-12}$), which will eventually allows $\varphi \rightarrow \chi\nu$ decay at temperature below neutrino decoupling temperature (~ 1 MeV). Non thermal decay of φ is the only source of DM(χ) production whereas φ freezes out thermally and gains non-zero number density via either of these two mechanisms : (i) the number changing self interactions ($3\varphi \rightarrow 2\varphi$), (ii) annihilation to SM particles ($2\varphi \rightarrow 2\text{SM}$). In this work we emphasise on the first scenario where φ has strong self interactions but very weak interaction with the SM bath. The implication of this particular scenario has been so far overlooked. Through our detailed numerical analysis we will highlight the importance of this mechanism in both DM phenomenology and its footprint on CMB. For the shake of completeness of the analysis, we will also consider the second process as well to showcase region of parameter space where these two scenarios are relevant.

It should be noted that in both cases φ particle maintain kinetic equilibrium with SM bath via the elastic scattering processes and share common temperature with SM bath contrary to studies that deal with secluded or decoupled dark sector scenarios [92, 93]. If the decay of φ is happening after neutrino decoupling then it will increase neutrino bath entropy and contribute to ΔN_{eff} . If the decay is completed before CMB we can trace the signature of DM from ΔN_{eff} at the time of CMB and find some interesting correlation of freeze in DM

and ΔN_{eff} in our proposed set up. Analogous scenarios of entropy injection between BBN and CMB epoch have been already investigated in various contexts. These include the consequence on priomodial nucleosynthesis resulting from the decay of non relativistic particle [94], the presence of relativistic dark matter from long lived state [95], and the contribution of dark radiation arising from decaying particle [96–99]. Although the aforementioned papers have conducted extensive analysis, most of them rely on a model independent formalism. In contrast, our analysis focuses on a specific particle physics model that aims to elucidate the observed DM relic density along with the production mechanism of DM. Among the examples listed above, only reference [95] discusses nonthermal DM, which can account for a small fraction ($\sim 1\%$) of the observed relic density. Conversely, our proposed framework provides nonthermal DM from the decay of self interacting heavier particle within the dark sector, providing a comprehensive explanation for the entire observed relic density.

The rest of the paper is structured as follows: In section II we introduce the model. The possible dynamics of DM production have been discussed in section III. In section IV we discuss the light neutrino production from late time decay of φ . The outcome of DM relic density together with the contribution to ΔN_{eff} at CMB for both scenarios-I and II have been discussed in section V. Finally, we summarize our results in section VI. We show relevant theoretical constraints and limit from the SM Higgs invisible decay width in Appendix A and Appendix B respectively. Feynman diagrams and corresponding thermal averaged cross-section for $3\varphi \rightarrow 2\varphi$ and $2\varphi \rightarrow 2\text{SM}$ processes are explicitly demonstrated in Appendix C and Appendix D respectively. A brief discussion on kinetic equilibrium is mentioned in Appendix E.

II. THE MODEL

In order to explain DM production from dark sector and its cosmological imprints in CMB, we extend the SM by a complex scalar φ , one Dirac fermion χ and three neutral Majorana fermions, $N_{1,2,3}$ which are singlet under the SM gauge group. An additional \mathcal{Z}_3 symmetry provides the stability of the lightest dark sector particle, under which the field φ and χ transform non-trivially i.e. $\{\varphi, \chi\} \rightarrow \{e^{i\frac{2\pi}{3}}\varphi, e^{i\frac{2\pi}{3}}\chi\}$ while all the SM fields including

$N_{1,2,3}$ transform trivially i.e. $\{N_{1,2,3}, \text{SM}\} \rightarrow \{N_{1,2,3}, \text{SM}\}$ ¹. The lightest dark state, χ acts as a stable DM candidate which is produced from the late time decay of the other dark sector particle, φ . The right handed neutrinos (RHN) i.e. $N_{1,2,3}$ which do not transform under \mathcal{Z}_3 , will be responsible for light neutrino mass via Type-I seesaw mechanism [14]. All the BSM fields and their corresponding charge assignments under the extended SM Electroweak (EW) gauge group are tabulated in table-I.

BSM Fields		$SU(2)_L$	$U(1)_Y$	\mathcal{Z}_3
Dark scalar (DS)	φ	1	0	$\omega(\equiv e^{i\frac{2\pi}{3}})$
DM	χ	1	0	$\omega(\equiv e^{i\frac{2\pi}{3}})$
RHN	$N_{1,2,3}$	1	0	1

TABLE I: Charge assignment of BSM fields under the extended SM EW gauge group, $\mathcal{G}_{\text{SM}}^{\text{EW}} \otimes \mathcal{Z}_3$.

The Lagrangian of this model takes the following form :

$$\mathcal{L} = \underbrace{\mathcal{L}_{\text{SM}}^{\text{K+Y}}}_{\text{SM}} - V(H) + \mathcal{L}_{\text{N}} + \mathcal{L}_{\text{DS}} + \mathcal{L}_{\text{DS-H}} + \mathcal{L}_{\text{DS-}\nu}. \quad (1)$$

Here, $V(H)$ represents the SM Higgs potential which is given by

$$V(H) = -\mu_H^2 |H|^2 + \lambda_H |H|^4. \quad (2)$$

The BSM part encapsulate interactions of heavy RHN sector (\mathcal{L}_{N}), dark sector (\mathcal{L}_{DS}) as well as their connection with the SM. The interaction of heavy RHN sector is described by,

$$\mathcal{L}_{\text{N}} = \sum_i i \bar{N}_i \gamma^\mu \partial_\mu N_i - \sum_{i,j} \frac{1}{2} M_{N_{ij}} \bar{N}_i^c N_j - \sum_{\ell,j} Y_{\ell j} \bar{L}_\ell \tilde{H} N_j + h.c. \quad (3)$$

where $i, j = 1, 2, 3$ and $\ell = e, \mu, \tau$ are lepton flavour indices. $L_\ell = (\nu_\ell \ \ell)^T$ are left handed the SM lepton doublet and H is the SM scalar doublet with $\tilde{H} = i\sigma_2 H^*$. The second term in eq.(3) is the Majorana mass term associated with $N_{1,2,3}$ and the last term is the Dirac Yukawa interactions with $N_{1,2,3}$. After electroweak symmetry breaking (EWSB), the SM scalar

¹ In general any \mathcal{Z}_N symmetry can serve similar kind of scenario with different self interacting number changing processes, $m \varphi \rightarrow 2 \varphi$ ($m \geq 3$), as well as the standard annihilation to SM particles, $2\varphi \rightarrow 2\text{SM}$. For example, \mathcal{Z}_2 will provide $4\varphi \rightarrow 2\varphi$ interactions which are more phase space suppressed for $M_\varphi \sim \mathcal{O}(\text{MeV})$ compare to $3\varphi \rightarrow 2\varphi$ interactions realised in \mathcal{Z}_3 symmetry [61].

doublet, H can be expressed in unitary gauge as $H = \begin{pmatrix} 0 \\ \frac{h+v}{\sqrt{2}} \end{pmatrix}^T$ where $v = 246$ GeV is vacuum expectation value (VEV) of SM Higgs. Active neutrino masses can be generated via Type-I seesaw mechanism followed from eq.(3) as $(m_\nu)_{3 \times 3} \approx (Yv/\sqrt{2})(M_N)^{-1}(Y^T v/\sqrt{2})$ and the mixing angle between active neutrino and RHN is then $\theta_{\text{mix}} \sim (Yv/\sqrt{2})(M_N)^{-1}$, where $M_N \approx (M_N)_{3 \times 3}$ [14].

The dark sector of this model consists of a complex scalar (φ) and a Dirac fermion (χ) with similar transformation property under \mathcal{Z}_3 . The lightest state behaves as a stable DM particle. The Lagrangian of the dark sector is described as follows:

$$\begin{aligned} \mathcal{L}_{\text{BSM}} &\supset \mathcal{L}_{\text{DS}} + \mathcal{L}_{\text{DS-H}} + \mathcal{L}_{\text{DS-}\nu} \\ &= \left(|\partial_\mu \varphi|^2 - \mu^2 |\varphi|^2 + i\bar{\chi}\gamma^\mu \partial_\mu \chi - M_{\text{DM}}\bar{\chi}\chi - \lambda_\varphi |\varphi|^4 - \frac{\mu_\varphi}{3!}(\varphi^3 + \varphi^{*3}) - y_{\varphi\chi}\bar{\chi}^c\chi\varphi \right) \\ &\quad + \left(-\lambda_{\varphi H}|H|^2|\varphi|^2 \right) + \left(-\sum_i y_{\varphi N_i}\bar{\chi}\varphi N_i + h.c. \right), \end{aligned} \quad (4)$$

where, $i = 1, 2, 3$. In the above equation, μ is the bare mass term of φ and M_{DM} is the mass of dark fermion χ . For simplicity, in this work we consider all parameters to be real. In the dark scalar sector, we assume $\mu > 0$ and $\lambda_\varphi > 0$ so that $\langle \varphi \rangle = 0$ which implies unbroken \mathcal{Z}_3 symmetry. After EWSB the physical mass of φ can be expressed as,

$$M_\varphi^2 = \mu^2 + \frac{\lambda_{\varphi H} v^2}{2}. \quad (5)$$

The most important interaction as far as our analysis is concerned, is given by the Yukawa interaction involving the dark scalar (φ), the DM (χ) and SM neutrinos (ν):

$$\mathcal{L}_{\text{DS-}\nu}^{\text{int}} = y_1 \bar{\chi}\nu\varphi + h.c. \quad (6)$$

This Lagrangian can be realized from the last term in braces in eq.(4) via small mixing angles(θ_{mix}) with RHNs($N_{1,2,3}$). The effective Yukawa coupling, y_1 can be understood as $\sum_i y_{\varphi N_i} \theta_{\text{mix}}^i$, where $i = 1, 2, 3$.

We choose our model parameters of the dark sector, in such a manner that we always get χ as the lightest dark sector particle. This mass pattern and the underlying discrete symmetry ensure us that the Dirac fermion (χ) with mass M_{DM} is the DM particle and φ with mass M_φ is the next to lightest particle (NLP) in this framework. The DM interacts with the SM bath only through φ via the Yukawa interaction shown in eq.(6). Thus for a given mass hierarchy between φ and χ , the life-time of φ is determined by the strength of the Yukawa coupling

y_1 . For our analysis, we assume NLP (φ) to be a long-lived ($\tau_\varphi > \tau_{\text{BBN}}$) particle and for this to happen one requires a very tiny Yukawa coupling $y_1 \lesssim 10^{-12}$ (for $M_\varphi \sim \mathcal{O}(\text{GeV})$). The NLP φ can be thermally produced via the sizable Higgs-portal interaction or through number changing self interaction processes. The production of the DM in the thermal bath through scattering process is highly suppressed because of its feeble coupling (y_1). However, it can be produced non-thermally from the decay of long-lived φ as shown in Fig.1. The

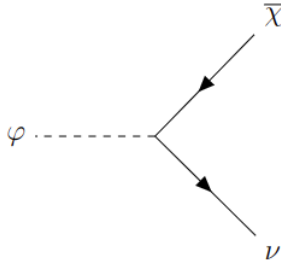


FIG. 1: *Diagram of DM production with active neutrinos from NLP φ*

decay width of φ to DM and a light neutrino is given by,

$$\Gamma_{\varphi \rightarrow \bar{\chi}\nu} = \frac{y_1^2 M_\varphi}{16\pi} \left(1 - \frac{M_{\text{DM}}^2}{M_\varphi^2}\right)^2. \quad (7)$$

Besides this, there are two more production channels of the DM χ : (a) $N_{1,2,3} \rightarrow \chi\varphi$ and (b) $\varphi \rightarrow \bar{\chi}^c\chi$. The main aim of this work is to connect non-thermal DM and ΔN_{eff} producing from self-interacting dark sector (NLP) which is achievable via the decay $\varphi \rightarrow \chi\nu$. But the presence of those new channels (a & b) will dilute the effect of the late time decay of φ in ΔN_{eff} and may even completely imperil our non-thermal dark matter scenario by thermalizing the dark sector. To avoid DM production from RHNs we set $M_{N_{1,2,3}} \gg T_{\text{RH}}$ so that their number densities get Boltzmann suppressed ($e^{-M_N/T}$) [88]. Therefore for our discussion, we choose the following hierarchy

$$M_{N_{1,2,3}} \gg T_{\text{RH}} > M_\varphi > M_{\text{DM}}. \quad (8)$$

In order to get active neutrino mass of the order ~ 0.1 eV, we require $M_{N_{1,2,3}} \sim \mathcal{O}(10^{10})$ GeV and $\theta_{\text{mix}} \sim \mathcal{O}(10^{-10})$ [100] and to satisfy the criteria of eq.8 we set $T_{\text{RH}} = 10^3$ GeV which is much above the current bound obtained from BBN [101]². Following this argument and

² The current lower bound on T_{RH} from BBN is few MeV [101] and successful baryogenesis is possible even with $T_{\text{RH}} \lesssim 100$ GeV [102, 103]. However, in that case one also has to set an upperbound on $M_\varphi \ll T_{\text{RH}}$

masses of relevant particles of this model, in the rest of our analysis we can safely ignore the production of DM from RHN decay in the computation of Y_φ and Y_χ . Moreover to suppress the process (b) we consider $y_{\varphi\chi} \ll y_1$, and this is necessary to exalt $\varphi \rightarrow \chi\nu$ decay so that φ can have the maximal contribution to ΔN_{eff} .

Interestingly, active neutrinos(ν) produced from the decay of NLP φ along with DM(χ) as shown in Fig.1 can have very intriguing consequences in the observation of CMB. We assume the value of Yukawa coupling (y_1) such that $\varphi \rightarrow \chi\nu$ decay mostly happens between neutrino decoupling temperature ($T < 2$ MeV) and CMB formation ($T \approx 0.1\text{eV}$). This promptly opens up the possibility of probing the impact of extra neutrino production from CMB radiation. And this can be achieved if y_1 varies in the range ($10^{-12} - 10^{-15}$) and for such a tiny coupling φ becomes a long-lived particle ($\tau_\varphi > \tau_{\text{BBN}}$). Thus the aforementioned supplementary active neutrino (ν) injection in our proposed scenario increases neutrino sector entropy and which in turn contribute significantly to additional neutrino degrees of freedom or ΔN_{eff} which is very precisely measured at the time of CMB. Thus any experimental observation on ΔN_{eff} can have very intriguing impact on the dynamics of dark scalar φ which in turn can influence the dark matter (χ) abundance via $\varphi \rightarrow \chi\nu$ decay process, thus affecting two disjoint (FIMP dark matter & N_{eff}) sectors simultaneously. To explore this phenomenology, we perform a detailed numerical scan over model parameters to show that the precise measurement of ΔN_{eff} at CMB can indeed restrict certain region of parameter space of non-thermal DM production which is otherwise remains elusive to visible sector due to extremely tiny strength of interactions involved in such non-thermal DM production process.

While doing our numerical analysis, we use the following model parameters:

$$\{M_{\text{DM}}, M_\varphi, \lambda_{\varphi H}, \lambda_\varphi, \mu_\varphi, y_1\}, \quad (9)$$

Here, the Higgs portal coupling $\lambda_{\varphi H}$ which decides the interaction between φ and SM, plays a significant role in deciding φ 's number density through $2\varphi \rightarrow 2$ SM annihilation and also in (φ SM $\rightarrow \varphi$ SM) elastic scattering processes. On the other hand, the scalar sector parameters λ_φ and μ_φ decide the self interactions of φ which is relevant for the number

in context of our analysis to get sufficient φ number density. On the other hand the effect of T_{RH} on primordial gravitational waves depends on specific inflationary model [104–106] whose analysis is beyond the scope of this work.

changing processes like $3\varphi \rightarrow 2\varphi$. And finally the effective Yukawa coupling, y_1 dictataes both DM abundance and additional contribution to N_{eff} .

III. DYNAMICS OF DARK SECTOR

In this section, we discuss the dynamics of the dark sector that leads to the early time production of the heavy NLP dark scalar (φ) followed by the late time non-thermal production of DM (χ) from the decay of φ . The number density of DM will be generated at some later epoch (after the neutrino decoupling temperature) of the Universe via the following two steps :

- Step I: *thermal production* of heavy dark scalar (φ) at the early time of Universe ($t < \tau_{\text{BBN}}$).
- Step II: *non-thermal production* of DM (χ) from the late time decay of φ ($\tau_{\text{BBN}} < t < \tau_{\text{CMB}}$).

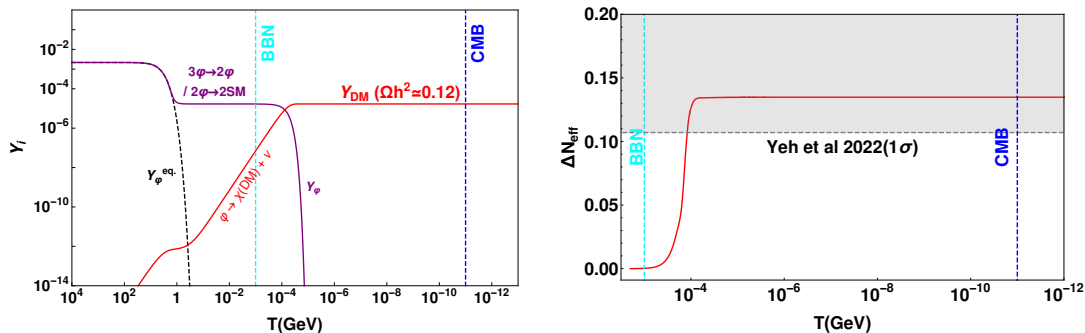


FIG. 2: A cartoon diagram of DM production(left) and the impact in ΔN_{eff} at the time of CMB(right).

A cartoon diagram of our proposed setup is shown in Fig.2. In the left panel, we show the variation of co-moving density as a function of temperature. The purple and red solid lines correspond to the thermal production of φ (Step I) and the non thermal production of DM (χ) (Step II) respectively. We also show two important temperatures, namely, the BBN and CMB that play crucial role in our analysis. Active neutrinos produced in the aforementioned decay of φ make substantial contributions to N_{eff} , which

can attract severe constraints from various observational limits on ΔN_{eff} , as shown in the right panel of Fig.2. The gray rectangular band is excluded by the limit obtained in Yeh et al at 1σ [78]. Having this broad picture in mind we now provide details of the thermal production of NLP followed by non-thermal production of DM in the rest of this section.

Step-I: Thermal production of φ

We consider a scenario in the early universe, when the interaction rate ($\Gamma_{\varphi}^{\text{int}}$) of the NLP (φ) dominates over the expansion rate (\mathcal{H}) of the Universe, ($\Gamma_{\varphi}^{\text{int}} \gg \mathcal{H}$) so that φ remains in thermal and chemical equilibrium. As the temperature of the universe cools down, the interaction rate of φ falls below the expansion rate of universe ($\Gamma_{\varphi}^{\text{int}} < \mathcal{H}$), thus the system departs from thermal equilibrium and the number density of φ freezes out. The number density of φ is mainly provided by the following two types of number changing processes: (i) $3\varphi \leftrightarrow 2\varphi$ via φ self interactions (shown in Fig.3(a)) and (ii) $2\varphi \leftrightarrow 2$ SM via the SM Higgs portal interactions (shown in Fig.3(b)). As a result of these two number changing processes, the NLP (φ) keeps its chemical equilibrium. On the other hand, the kinetic equilibrium is maintained between φ and the SM bath via elastic scatterings, generically expressed as $\varphi \text{ SM} \leftrightarrow \varphi \text{ SM}$ which help φ to keep same temperature with SM bath till freeze out takes place.

The complete dynamics of thermal production of φ can be described by the following Boltzmann equation:

$$\begin{aligned} \frac{dY_{\varphi}}{dx} = & -0.116 \frac{g_s^2}{\sqrt{g_{\rho}}} \frac{M_{\varphi}^4}{x^5} M_{pl} \langle \sigma v^2 \rangle_{3\varphi \rightarrow 2\varphi} (Y_{\varphi}^3 - Y_{\varphi}^2 Y_{\varphi}^{eq}) \\ & -0.264 \frac{g_s}{\sqrt{g_{\rho}}} \frac{M_{\varphi}}{x^2} M_{pl} \langle \sigma v \rangle_{2\varphi \rightarrow 2\text{SM}} (Y_{\varphi}^2 - Y_{\varphi}^{eq2}) \\ & - \sqrt{\frac{45}{4\pi^3}} \langle \Gamma_{\varphi \rightarrow \chi\nu} \rangle \frac{x}{M_{\varphi}^2} \frac{M_{pl}}{\sqrt{g_{\rho}}} Y_{\varphi} . \end{aligned} \quad (10)$$

Let us first describe various notations used in eq.(10). $Y_{\varphi}(= \frac{n_{\varphi}}{s})$ is the co-moving number density of φ where s is the entropy density and x is the dimensionless parameter defined as $x = \frac{M_{\varphi}}{T}$. Y_{φ}^{eq} is the equilibrium co-moving number density of φ . $g_s(x)$ and $g_{\rho}(x)$ are the effective relativistic degrees of freedom associated with entropy density and the energy density respectively and finally M_{pl} is the Planck mass ($M_{pl} = 1.22 \times 10^{19} \text{GeV}$). The thermal averaged cross-section of $2\varphi \rightarrow 2$ SM process is denoted by $\langle \sigma v \rangle_{2\varphi \rightarrow 2\text{SM}}$ and for self-interacting number changing process ($3\varphi \rightarrow 2\varphi$), it is defined as $\langle \sigma v^2 \rangle_{3\varphi \rightarrow 2\varphi}$. The first two terms in

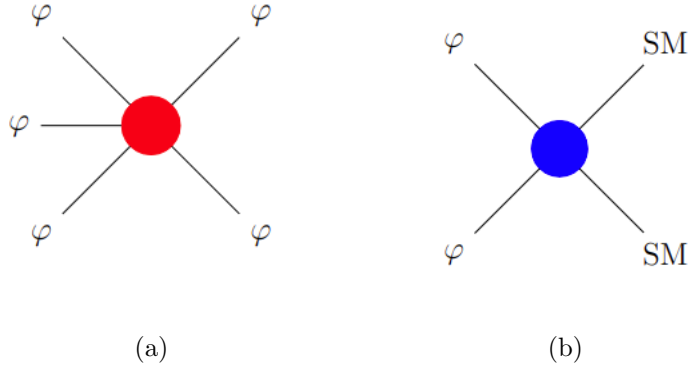


FIG. 3: A cartoon of number changing process of φ : (a) three φ annihilate to two φ ($3\varphi \rightarrow 2\varphi$). and (b) two φ annihilate to two SM particles ($2\varphi \rightarrow 2\text{SM}$).

eq.(10) lead to non zero density of φ via thermal freeze-out mechanism and it occurs at $x = x_F^{\text{tot}}$, where **tot** in the superscript implies that both number changing processes i.e. $3\varphi \rightarrow 2\varphi$ and $2\varphi \rightarrow 2\text{SM}$ are involved in φ freeze-out process. The last term in eq.(10) provides the late time (after BBN) decay of φ into DM (χ) and SM neutrinos, resulting the dilution of number density of φ into χ and ν .

From eq.(10) it is clear that two number changing processes of NLP (φ) as discussed above are present to keep φ in the thermal bath. However, depending upon the mass and couplings of NLP, it can be shown very easily that one of those two number changing processes is infact sufficient for the freeze-out and the final yield of NLP (φ). To justify our argument quantitatively we define the interaction rate of $3\varphi \rightarrow 2\varphi$ process as: $\Gamma_{3\varphi \rightarrow 2\varphi} = n_\varphi^2 \langle \sigma v^2 \rangle_{3\varphi \rightarrow 2\varphi}$ and of $2\varphi \rightarrow 2\text{SM}$ as: $\Gamma_{2\varphi \rightarrow 2\text{SM}} = n_\varphi \langle \sigma v \rangle_{2\varphi \rightarrow 2\text{SM}}$. In addition to these number changing processes, the number preserving scattering process ($\varphi \text{ SM} \rightarrow \varphi \text{ SM}$) is also present to keep φ in kinetic equilibrium with SM bath. The interaction rate of this process is defined as: $\Gamma_{[\varphi \text{ SM} \rightarrow \varphi \text{ SM}]} = n_{\text{SM}} \langle \sigma v \rangle_{[\varphi \text{ SM} \rightarrow \varphi \text{ SM}]}$. Depending on the relative interaction strength between two number changing processes of φ , we are interested in the following two production modes of φ :

$$\text{Scenario I : } \Gamma_{[\varphi \text{ SM} \rightarrow \varphi \text{ SM}]} > \Gamma_{3\varphi \rightarrow 2\varphi} \gg \Gamma_{2\varphi \rightarrow 2\text{SM}} ,$$

$$\text{Scenario II : } \Gamma_{[\varphi \text{ SM} \rightarrow \varphi \text{ SM}]} > \Gamma_{2\varphi \rightarrow 2\text{SM}} \gg \Gamma_{3\varphi \rightarrow 2\varphi} .$$

In the above hierarchy of scattering processes, $\Gamma_{[\varphi \text{ SM} \rightarrow \varphi \text{ SM}]}$ plays a decisive part in maintaining kinetic equilibrium of φ . During the freeze-out of φ through processes like: $n\varphi \rightarrow 2\varphi$,

(for $n > 2$) the rest mass energy of initial state particles can significantly enhance the kinetic energy of final state particles, which in turn can heat up the dark sector [68], leading to an imbalance between the dark sector temperature (T_φ) and SM bath temperature (T). Thus, in general, to take into account this temperature imbalance one should consider a new parameter (T_φ) in the evolution equation of NLP number density (Y_φ) [88]. However, in our study we can avoid this paradigm by considering kinetic equilibrium between φ and SM bath, i.e. by taking $T_\varphi = T$ at least upto the temperature at which φ freezes out from the thermal bath. And to achieve this, $\Gamma_{[\varphi \text{ SM} \rightarrow \varphi \text{ SM}]}$ must be larger than interaction rate of the other processes as well as the expansion rate \mathcal{H} of the universe (i.e $\Gamma_{[\varphi \text{ SM} \rightarrow \varphi \text{ SM}]|_{x_F} \gtrsim \mathcal{H}(x_F)$) [67]. Most importantly this condition must be satisfied in both Scenario I and II. The relevant Feynman diagrams and thermal averaged cross-sections for $3\varphi \rightarrow 2\varphi$, $2\varphi \rightarrow 2\text{SM}$ and $\varphi \text{ SM} \rightarrow \varphi \text{ SM}$ processes are shown in Appendices C and D.

- **Scenario I:** In this scenario we consider the interaction rate of $3\varphi \rightarrow 2\varphi$ number changing process ($\Gamma_{3\varphi \rightarrow 2\varphi}$) is significantly higher than $2\varphi \rightarrow 2\text{SM}$ process ($\Gamma_{2\varphi \rightarrow 2 \text{SM}}$). Thus $3\varphi \rightarrow 2\varphi$ process successfully keeps φ in thermal bath for longer duration in comparison to the process $2\varphi \rightarrow 2 \text{SM}$. Hence freeze-out of φ is mainly governed by the $3\varphi \rightarrow 2\varphi$ process and it occurs at $x = x_F^{3\varphi \rightarrow 2\varphi} \approx x_F^{\text{tot}} > x_F^{2\varphi \rightarrow 2\text{SM}}$. Here $x_F^{3\varphi \rightarrow 2\varphi}$ ($x_F^{2\varphi \rightarrow 2\text{SM}}$) signifies the inverse freeze out temperature of φ when only $3\varphi \rightarrow 2\varphi$ ($2\varphi \rightarrow 2\text{SM}$) is considered.

In our model, the interaction rate of $3\varphi \rightarrow 2\varphi$ ($2\varphi \rightarrow 2\text{SM}$) process depends on the couplings $\lambda_\varphi, \mu_\varphi/M_\varphi$ ($\lambda_{\varphi H}$) and mass M_φ . To demonstrate the dynamics (where $\Gamma_{3\varphi \rightarrow 2\varphi} \gg \Gamma_{2\varphi \rightarrow 2 \text{SM}}$), we show the variation of the co-moving number density Y_φ as a function of $x(= M_\varphi/T)$ in Fig.4(a) for a sample Benchmark point: $\{M_\varphi, \mu_\varphi/M_\varphi, \lambda_{\varphi H}, \lambda_\varphi\} = \{20 \text{ GeV}, 0.1, 10^{-2}, 1\}$. The black solid line corresponds to the equilibrium co-moving density of φ (Y_φ^{eq}) and the blue dashed line corresponds to the co-moving number density of φ considering contributions from both the number changing processes: $3\varphi \rightarrow 2\varphi$ and $2\varphi \rightarrow 2 \text{SM}$ in eq.(10). The brown solid line (red dotted line) depicts the variation of number density of φ when only $3\varphi \rightarrow 2\varphi$ ($2\varphi \rightarrow 2 \text{SM}$) process is present in eq.(10). The relative contribution of these two processes in the evolution of Y_φ is clearly seen in this figure. If we consider only the sub-dominant $2\varphi \rightarrow 2 \text{SM}$ process, φ freezes-out earlier (red dotted line) due to small

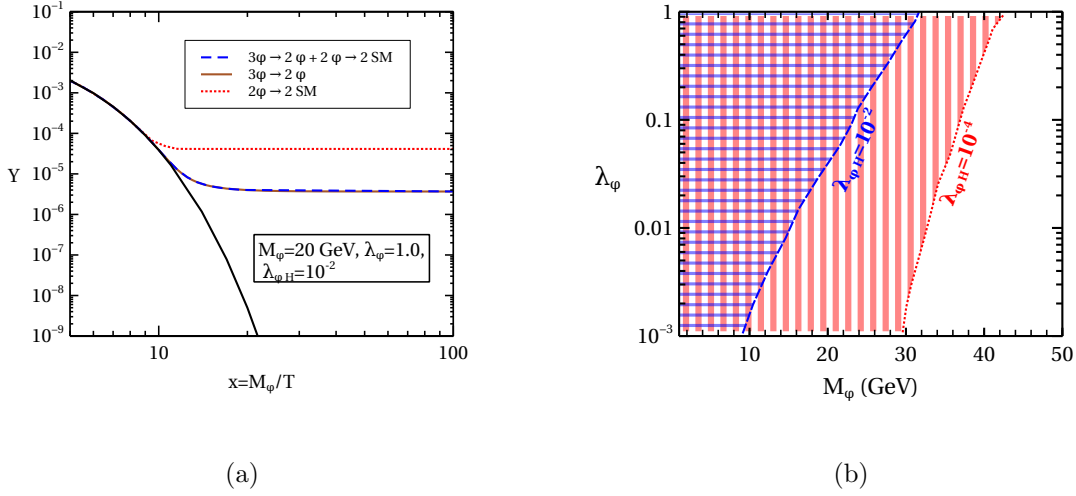


FIG. 4: (a) Thermal freeze-out of φ for $M_\varphi = 20$ GeV, $\mu_\varphi/M_\varphi = 0.1$, $\lambda_{\varphi H} = 10^{-2}$, $\lambda_\varphi = 1.0$. The black solid line signifies Y_φ^{eq} . The blue dashed line corresponds to Y_φ considering contributions from both $3\varphi \rightarrow 2\varphi$ and only $2\varphi \rightarrow 2$ SM processes. The brown solid line and red dotted line represent Y_φ considering only $3\varphi \rightarrow 2\varphi$ and $2\varphi \rightarrow 2$ SM process respectively. (b) Parameter space for scenario-I in M_φ vs. λ_φ plane with $\mu_\varphi/M_\varphi = 0.1$ for two different values of $\lambda_{\varphi H} = \{10^{-2}, 10^{-4}\}$ depicted by the blue and red shaded region respectively. The criteria for scenario-I holds only for the region left to individual lines where x_F^{tot} is governed by $3\varphi \rightarrow 2\varphi$ process.

$\Gamma_{2\varphi \rightarrow 2 \text{ SM}}$, whereas, the dominant $3\varphi \rightarrow 2\varphi$ process maintains φ in thermal bath for longer duration (brown solid line). Thus the freeze-out abundance of φ (blue dashed line) is governed mainly by the dominant $3\varphi \rightarrow 2\varphi$ process due to larger $\Gamma_{3\varphi \rightarrow 2\varphi}$ for our choice of model parameters. Therefore, we can safely ignore the second term in eq.(10) and the modified Boltzmann equation takes the following form:

$$\begin{aligned} \frac{dY_\varphi}{dx} = & -0.116 \frac{g_s^2}{\sqrt{g_\rho}} \frac{M_\varphi^4}{x^5} M_{pl} \langle \sigma v^2 \rangle_{3\varphi \rightarrow 2\varphi} (Y_\varphi^3 - Y_\varphi^2 Y_\varphi^{eq}) \\ & - \sqrt{\frac{45}{4\pi^3}} \langle \Gamma_{\varphi \rightarrow \chi\nu} \rangle \frac{x}{M_\varphi^2} \frac{M_{pl}}{\sqrt{g_\rho}} Y_\varphi. \end{aligned} \quad (11)$$

Based on the above argument we can identify the parameter space for scenario-I satisfying the criteria: $x_F^{3\varphi \rightarrow 2\varphi} > x_F^{2\varphi \rightarrow 2\text{SM}}$. In Fig.4(b) we display the parameter space for this scenario in M_φ vs. λ_φ plane with $\mu_\varphi/M_\varphi = 0.1$ for two different values $\lambda_{\varphi H} = \{10^{-2}, 10^{-4}\}$ depicted by the blue and red shaded region respectively. The criteria for scenario-I holds only for the region left to individual lines. With an increase

in M_φ , $\Gamma_{3\varphi \rightarrow 2\varphi}$ becomes more mass suppressed compared to $\Gamma_{2\varphi \rightarrow 2\text{SM}}$. Hence for fixed values of λ_φ , and $\lambda_{\varphi H}$ with increasing M_φ , $\Gamma_{3\varphi \rightarrow 2\varphi}$ falls below $\Gamma_{2\varphi \rightarrow 2\text{SM}}$ and scenario-I doesn't hold anymore for the parameter space right to the colored lines. With an increase in $\lambda_{\varphi H}$, $\Gamma_{2\varphi \rightarrow 2\text{SM}}$ increases and eventually $\Gamma_{3\varphi \rightarrow 2\varphi}$ falls below $\Gamma_{2\varphi \rightarrow 2\text{SM}}$ even with lower M_φ . For that reason we see the shaded region moves toward lower M_φ (towards left) with an increase in $\lambda_{\varphi H}$. The regions right to the colored lines demand a different treatment which will be discussed shortly.

Before we conclude this part of our analysis, it is worth noting that the present dark sector dynamics also allows $4\varphi \rightarrow 2\varphi$ number changing process involving the same λ_φ coupling that is responsible for $3\varphi \rightarrow 2\varphi$ process. In spite of the same interaction strength (λ_φ), $4\varphi \rightarrow 2\varphi$ process is more phase space suppressed compared to that of $3\varphi \rightarrow 2\varphi$, hence, we neglect it in our numerical calculation of Y_φ .

- **Scenario II:** In this picture we consider $\Gamma_{2\varphi \rightarrow 2\text{SM}} \gg \Gamma_{3\varphi \rightarrow 2\varphi}$, which is contrary to the previous scenario. In this case freeze-out of φ is dictated by $2\varphi \rightarrow 2\text{SM}$ annihilation process that keeps φ in thermal bath for a longer period compared to $3\varphi \rightarrow 2\varphi$ process. Hence the freeze-out of φ occurs at $x = x_F^{\text{tot}} \approx x_F^{2\varphi \rightarrow 2\text{SM}} > x_F^{3\varphi \rightarrow 2\varphi}$.

In Fig.5(a) we report the evolution of Y_φ as a function of $x = \frac{M_\varphi}{T}$ for $\lambda_\varphi = 0.01$ keeping other parameters same as in Scenario-I. From this figure it is evident that Y_φ is entirely decided by $2\varphi \rightarrow 2\text{SM}$ number changing processes contrary to the previous scenario where $3\varphi \rightarrow 2\varphi$ process was controlling the dynamics. Thus eq.(10) can be simplified by neglecting the sub-dominant $3\varphi \rightarrow 2\varphi$ process:

$$\begin{aligned} \frac{dY_\varphi}{dx} = & -0.264 \frac{g_s}{\sqrt{g_\rho}} \frac{M_\varphi}{x^2} M_{pl} \langle \sigma v^2 \rangle_{2\varphi \rightarrow 2\text{SM}} (Y_\varphi^2 - (Y_\varphi^{eq})^2) \\ & - \sqrt{\frac{45}{4\pi^3}} \langle \Gamma_{\varphi \rightarrow \chi\nu} \rangle \frac{x}{M_\varphi^2} \frac{M_{pl}}{\sqrt{g_\rho}} Y_\varphi. \end{aligned} \quad (12)$$

In Fig.5(b) we display parameter space for this scenario in M_φ vs. $\lambda_{\varphi H}$ plane with $\mu_\varphi/M_\varphi = 0.1$ for two different values $\lambda_\varphi = (10^{-1} \ \& \ 10^{-2})$ depicted by the blue and red shaded region respectively. For the same reason discussed in the context of scenario-I, in this case also $\Gamma_{3\varphi \rightarrow 2\varphi}$ decreases with decrease in λ_φ and finally falls below $\Gamma_{2\varphi \rightarrow 2\text{SM}}$. And this phenomena is true even for lower M_φ . For this reason here also we see that the shaded region shifts towards lower M_φ (left) with decrease in λ_φ .

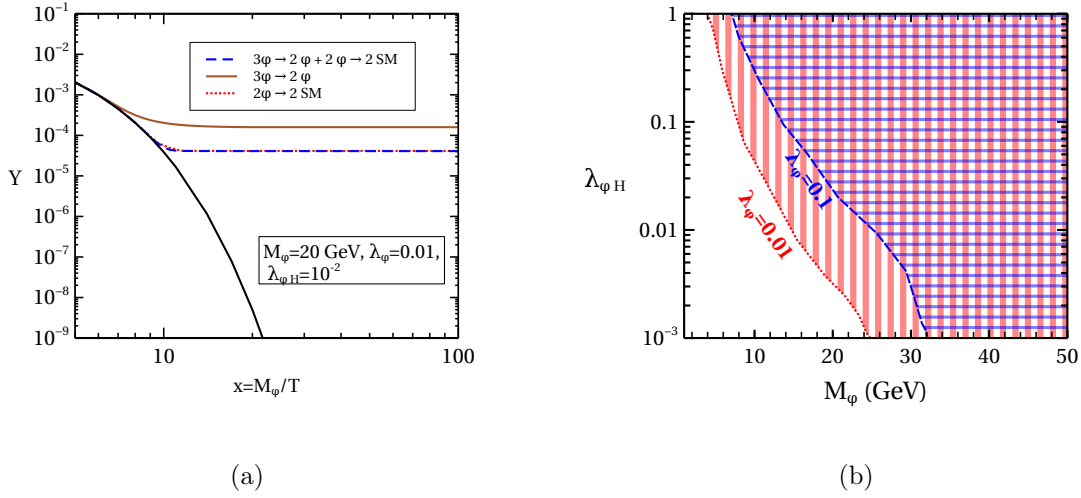


FIG. 5: (a) Thermal freeze-out of φ for $M_\varphi = 20$ GeV, $\mu_\varphi/M_\varphi = 0.1$, $\lambda_{\varphi H} = 10^{-2}$, $\lambda_\varphi = 0.1$. The black solid line signifies Y_φ^{eq} . The blue dashed line corresponds to Y_φ considering contributions from both $3\varphi \rightarrow 2\varphi$ and only $2\varphi \rightarrow 2$ SM processes. The brown solid line and red dotted line represent Y_φ considering only $3\varphi \rightarrow 2\varphi$ and $2\varphi \rightarrow 2$ SM process respectively. (b) Parameter space for scenario-II in M_φ vs. λ_φ plane with $\mu_\varphi/M_\varphi = 0.1$ for two different values of $\lambda_{\varphi H} = \{10^{-2}, 10^{-4}\}$ depicted by the blue and red shaded region respectively. The criteria for scenario-II holds only for the region right to individual lines where x_F^{tot} is governed by $2\varphi \rightarrow 2$ SM process.

In summary the main observation of this whole subsection are the following:

$$\begin{aligned}
 \text{Scenario I : } & \Gamma_{3\varphi \rightarrow 2\varphi} \gg \Gamma_{2\varphi \rightarrow 2\text{SM}} \implies x_F^{\text{tot}} \approx x_F^{3\varphi \rightarrow 2\varphi} > x_F^{2\varphi \rightarrow 2\text{SM}}, \\
 \text{Scenario II : } & \Gamma_{3\varphi \rightarrow 2\varphi} \ll \Gamma_{2\varphi \rightarrow 2\text{SM}} \implies x_F^{\text{tot}} \approx x_F^{2\varphi \rightarrow 2\text{SM}} > x_F^{3\varphi \rightarrow 2\varphi}.
 \end{aligned} \tag{13}$$

It is worth mentioning that scenario-II is more common and has already been studied in different literature [59, 87], where mother particles are considered to have sizable annihilation cross-section with SM bath. In this work our main focus is on scenario-I, although for the sake of completeness of the analysis we also discuss scenario-II.

Step-II: Non thermal DM production

Following our previous discussion we now focus on the non-thermal production of DM (χ) from the dilution of φ density described by the last term in the R.H.S of eq.(10). We

solve the following Boltzmann equation to get the evolution of DM(χ) abundance,

$$\frac{dY_\chi}{dx} = \sqrt{\frac{45}{4\pi^3}} \langle \Gamma \rangle_{\varphi \rightarrow \chi\nu} \frac{x}{M_{sc}^2} \frac{M_{pl}}{\sqrt{g_\rho}} Y_\varphi, \quad (14)$$

where, Y_χ is the co-moving number density of DM χ . In general, the solution of Y_φ comes from eq.(11) for scenario-I and in eq.(12) for scenario-II respectively. In the calculation of $\Gamma(\varphi \rightarrow \chi\nu)$ we consider the Yukawa coupling y_1 in the range ($\sim 10^{-12} - 10^{-15}$) so that the decay of $\varphi \rightarrow \chi + \nu$ happens in post BBN and pre CMB era. At this stage, we find it worth discussing one subtle issue regarding the thermal averaged decay width $\langle \Gamma \rangle_{\varphi \rightarrow \chi\nu}$. As we have pointed out before, that at the time when φ freezes-out, it maintains the same temperature as the SM bath via the elastic scattering processes. However the condition for kinetic equilibrium holds only upto freeze out and is no longer maintained at the time of decay ($< T_{\text{BBN}}$) as shown in Appendix E. This results the dark sector to acquire a different temperature T' ($\neq T$) than the thermal bath and this must be evaluated in order to get $\langle \Gamma \rangle_{\varphi \rightarrow \chi\nu}$. In this work, as we are studying the dark sector dynamics at low temperature ($T' \ll M_\varphi$), and in this limit the thermally averaged decay width can simply be approximated as $\langle \Gamma \rangle_{\varphi \rightarrow \chi\nu}(T') \approx \Gamma_{\varphi \rightarrow \chi\nu}$ [42, 107], thus reducing the complication of tracking temperature dependence of the evolution of φ . After solving eq.(14) we get the complete picture of DM production as shown by red solid line in the left panel of Fig.2.

IV. LIGHT NEUTRINO PRODUCTION BEFORE CMB

Now we discuss the production of supplementary light neutrinos from the late time decay of φ and the relevant mechanism of verifying those light degrees of freedom at CMB. As revealed earlier, neutrinos that are produced after neutrino decoupling ($T \lesssim 2$ MeV) would inject entropy in the neutrino bath. At the time of CMB, the number of relativistic neutrino degrees of freedom is expressed as,

$$N_{\text{eff}}^{\text{CMB}} = \frac{8}{7} \left(\frac{11}{4} \right)^{4/3} \frac{\rho_\nu^{\text{SM}}}{\rho_\gamma} \Bigg|_{T=T_{\text{CMB}}}, \quad (15)$$

where, $\rho_\nu^{\text{SM}} = 3 \times 2 \times \frac{7}{8} \times \frac{\pi^2}{30} (T_\nu^{\text{SM}})^4$ and $\rho_\gamma = 2 \times \frac{\pi^2}{30} T^4$ are energy densities of neutrino and photon respectively. Due to the extra neutrino injection from the non-thermal decay of φ , the energy density of the neutrino bath increases to ρ'_ν ($\rho'_\nu > \rho_\nu^{\text{SM}}$). In this case, the

relativistic neutrino degrees of freedom (N'_{eff}) also differs from the prediction of SM at the time of CMB. We parameterise this deviation at the time of CMB in the following manner,

$$\Delta N_{\text{eff}} = \left(\frac{\rho'_\nu}{\rho_\nu^{\text{SM}}} - 1 \right) N_{\text{eff}}^{\text{SM}} \Big|_{T=T_{\text{CMB}}} . \quad (16)$$

We now solve the following Boltzmann equation to estimate the evolution of ρ'_ν with temperature,

$$\frac{d\rho'_\nu}{dx} = -\frac{4\beta\rho'_\nu}{x} + \frac{1}{xH(x)} \langle E\Gamma \rangle_{\varphi \rightarrow \chi\nu} Y_\varphi s , \quad (17)$$

where the term β indicates the variation of $g_s(T)$ with T and is defined as

$$\beta(T) = 1 + \frac{1}{3} \frac{T}{g_s(T)} \frac{dg_s(T)}{dT} . \quad (18)$$

where, x is the dimensionless variable as mentioned earlier in context of equation (10). Y_φ is the co-moving number density of φ which is computed by solving eq.(11) or eq.(12) depending on the scenario we consider. $g_s(x)$ is the number of effective degrees of freedom related to the entropy density and s is the co-moving entropy density. The term $\langle E\Gamma \rangle_{\varphi \rightarrow \chi\nu}$ in eq.(17) is the most crucial ingredient in this analysis which represents the thermal averaged energy density transferred to neutrino sector and is defined as

$$\langle E\Gamma \rangle_{\varphi \rightarrow \chi\nu} = \frac{|\mathcal{M}|_{\varphi \rightarrow \chi\nu}^2 (M_\varphi^2 - M_{\text{DM}}^2)}{32\pi M_\varphi^2} \left(1 - \frac{M_{\text{DM}}^2}{M_\varphi^2} \right) .$$

The first term in the R.H.S of eq.(17) is responsible for the dilution of ρ'_ν due to expansion of the universe while the second term decides the evolution of augmented contribution to ρ'_ν from φ decay. The evolution of ρ_ν^{SM} after the decoupling of neutrinos is governed by only the expansion effect. Thus in the absence of any new source ρ_ν^{SM} can be computed by setting the second term of the R.H.S of eq.(17) equal to zero and considering only the dilution of energy density.

V. RELIC DENSITY AND ΔN_{eff}

So far we have built up the basic framework of the underlying dynamics of dark sector particles (φ and χ) that provided freeze-in DM as well as yielded extra active light neutrino that with its possible footprints in ΔN_{eff} . In this section, we perform an exhaustive numerical analysis of Scenario-I and Scenario-II to quantitatively estimate phenomenological

consequences of the late-time decay of φ in the light of current and future measurements of ΔN_{eff} . For this we first scrutinize the dependence of DM relic density and the ΔN_{eff} on various model parameters as elaborated in sec-III and sec-IV respectively.

A. Relic density

To calculate the DM relic density, we numerically solve eq.(14) along with either eq.(11) (for scenario-I) or eq.(12) (for scenario-II). The solution of the coupled Boltzmann equations for each scenario yields Y_φ and Y_χ as a function of $x(= M_\varphi/T)$. Using the co-moving density of DM, Y_χ at $x \rightarrow \infty$, one finds out DM relic density as [23]:

$$\Omega_\chi h^2 = 2.755 \times 10^8 \times \left(\frac{M_{\text{DM}}}{\text{GeV}} \right) \times Y_\chi^{\text{today}}, \quad (19)$$

where $Y_\chi^{\text{today}} = Y_\chi(x \rightarrow \infty)$. The precise determination of Y_χ^{today} is highly model dependent. In the following two sub-sections we pin down Y_χ^{today} for scenario-I and II and corresponding relic densities.

Scenario-I: As shown before, densities of φ and χ for the scenario-I are mainly driven by $3\varphi \rightarrow 2\varphi$ number changing process in the dark scalar sector. Based on this number changing process, we calculate the co-moving abundances of φ and χ and show their evolution with $x(= M_\varphi/T)$ in Fig.6. The solid, dashed and dotted lines signify Y_φ , Y_φ^{eq} and Y_χ respectively. It can be seen from these figures that the late-time decay of φ (solid lines) produces the abundance of χ . As the $\varphi \rightarrow \chi + \nu$ decay proceeds, the number density of φ slowly changes into χ number density and eventually at the end of the decay, the density of φ completely dilutes to χ number density ($Y_\chi \equiv Y_\varphi$ at $\tau \gg \tau_\varphi$). One can easily understand this from the fact that $\varphi \rightarrow \chi\nu$ decay is the only possible decay mode of the NLP (φ) [108]. Thus, in the generation of Y_χ from Y_φ , the magnitude of the Yukawa coupling ($y_1 > 0$) has hardly any role to play, except for setting the lifetime of φ and this provides $Y_\varphi(x_F^{3\varphi \rightarrow 2\varphi}) \simeq Y_\chi^{\text{today}}$. Therefore the relic density of DM given in eq.(19) turns out to be $\Omega_\chi h^2 \propto M_{\text{DM}} \times Y_\varphi(x_F^{3\varphi \rightarrow 2\varphi})$. Consequently in order to get fixed $\Omega_\chi h^2$, any increase in M_{DM} demands a decrease in $Y_\varphi(x_F^{3\varphi \rightarrow 2\varphi})$ and vice versa. We have pointed out before that $\varphi \rightarrow \chi \nu$ decay to happen between BBN and CMB the value of y_1 should lie in the range : $\{10^{-12} - 10^{-15}\}$. As a sample representative value we set $y_1 = 10^{-12}$ throughout our numerical analysis. To show the evolution of Y_φ and Y_χ with temperature, we fix $\mu_\varphi/M_\varphi = 0.1$ and $M_{\text{DM}} = 400$

keV for both plots. We consider $\lambda_{\varphi H} = 10^{-4}$ to realize Scenario-I.

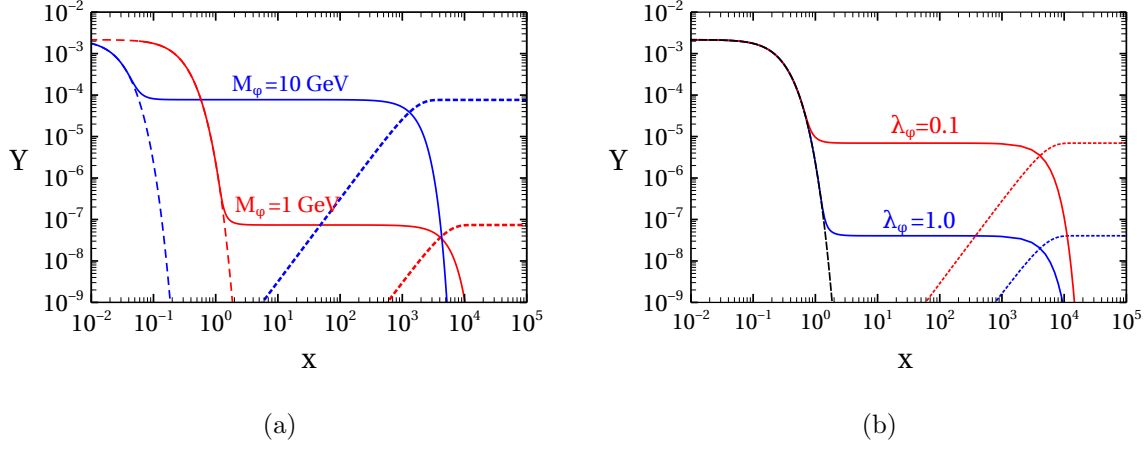


FIG. 6: *Evolution of co-moving abundances of φ (solid line) and $DM(\chi)$ (dotted line) with $x(\equiv 1/T)$ (T in GeV) for scenario-I. In (a) for a fixed $\lambda_\varphi = 1.0$ with two different values of M_φ and in (b) for a fixed $M_\varphi = 1$ GeV with two different values of λ_φ are shown. The Higgs portal coupling is considered here to small, $\lambda_{\varphi H} = 10^{-4}$ in order to realise the scenario. The other parameters like $y_1 = 10^{-12}$, $M_{DM} = 400$ keV and $\mu_\varphi/M_\varphi = 0.1$ are kept same for both plots.*

In Fig.6(a) we present evolution of densities Y_φ (solid line) and Y_χ (dotted line) as a function of dimension less parameter $x(= M_\varphi/T)$ for two different M_φ and a fixed self-interaction coupling $\lambda_\varphi = 1.0$. The dynamics of dark sector particles for $M_\varphi = 1$ GeV and $M_\varphi = 10$ GeV are depicted by red and blue colors respectively. With the increase of M_φ , $\langle\sigma v^2\rangle_{3\varphi\rightarrow 2\varphi}$ encounters phase space and propagator suppression which is also understood from the expression given in appendix C. As Y_φ goes like $Y_\varphi \propto 1/\langle\sigma v^2\rangle_{3\varphi\rightarrow 2\varphi}$ (using analytical solution [63]), with the smaller $\langle\sigma v^2\rangle_{3\varphi\rightarrow 2\varphi}$, the thermal freeze-out of φ happens at earlier time with higher abundance Y_φ and eventually this Y_φ is transferred to the Y_χ . As a result Y_χ is also higher for higher M_φ . This feature is portrayed in the Fig.6(a) where higher(lower) value of M_φ leads to the higher(lower) abundance Y_χ represented by the red(blue) dotted line.

To study the role of dark scalar self-coupling, λ_φ on DM abundance, in Fig.6(b) we show the variation in Y_χ for two different values of $\lambda_\varphi = 0.1$ (red line) and 1.0 (blue line) keeping $M_\varphi = 1$ GeV. It is obvious, that as the value of λ_φ increases, the thermal averaged cross-section $\langle\sigma v^2\rangle_{3\varphi\rightarrow 2\varphi}$ also increases which eventually reduces the abundance Y_φ and finally this reduced Y_φ generates lower Y_χ . This is elucidated in Fig.6(b), where a higher(lower) value

of λ_φ gives a lower(higher) Y_χ as it is shown by the blue(red) dotted line.

The other parameter μ_φ with mass dimension, is also responsible for $3\varphi \rightarrow 2\varphi$ processes as $\langle\sigma v^2\rangle_{3\varphi\rightarrow 2\varphi} \propto (\mu_\varphi/M_\varphi)^2$ (see Appendix C). With an increase in the ratio μ_φ/M_φ , the cross-section will enhance leading to a decrease in Y_φ as well as Y_χ . For simplicity, we consider the ratio $\mu_\varphi/M_\varphi = 0.1$ throughout our analysis and is consistent with the theoretical upper bound on μ_φ coming from stable vacuum as discussed in Appendix A.

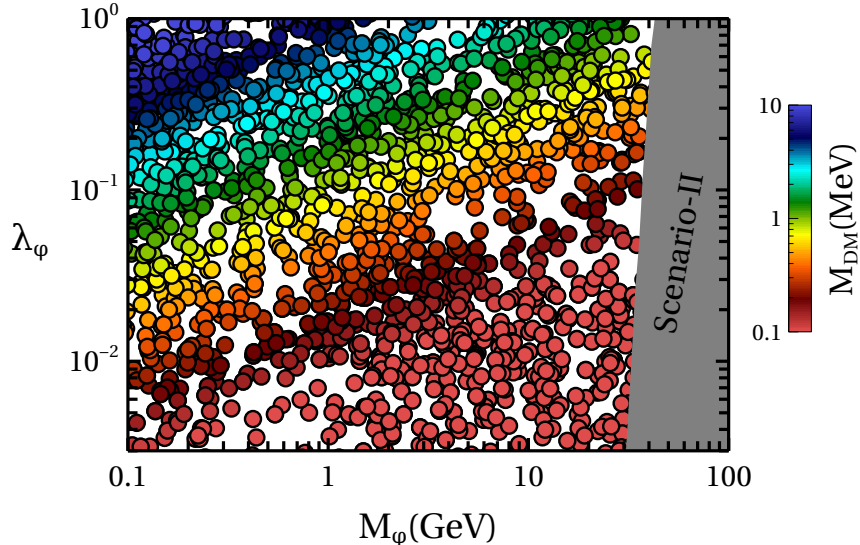


FIG. 7: *DM relic density satisfied points in $M_\varphi - \lambda_\varphi$ plane for scenario-I with $\mu_\varphi/M_\varphi = 0.1$, $\lambda_{\varphi H} = 10^{-4}$ and $y_1 = 10^{-12}$. The color gradient indicates the range of M_{DM} satisfying the correct relic density. The shaded region corresponds to the parameter space where scenario-II is dominating over scenario-I. White regions are just computational artifact associated with the scan.*

After describing the dependence of relic abundance on different model parameters, we now present the allowed region of dark sector parameter space from DM observed density, ($\Omega_{\text{DM}}h^2 = 0.120 \pm 0.001$) given by PLANCK [6]. We perform a numerical scan on the model parameters in the following range

$$M_\varphi : \{0.1 - 100 \text{ GeV}\}, \quad \lambda_\varphi : \{0.001 - 1\}; \quad (20)$$

to calculate $\Omega_\chi h^2$ using eq.(19). We keep other parameters fixed as in Fig.6. and to allow the on shell decay $\varphi \rightarrow \chi + \nu$ we set $M_\varphi > M_{\text{DM}}$.

Our scan result is displayed in Fig.7, where we show points satisfying relic density constraints in λ_φ vs. M_φ plane. The grey shaded region corresponds to the parameter space where scenario-II dominates which demands a different analysis and will be discussed shortly. The color gradient in the above figure represents DM mass range varying from 0.1 MeV to 10 MeV set by the observed relic density constraint. One can see from this figure that the higher value of λ_φ prefers to higher value of M_{DM} . As explained in the context of Fig.6, with the increase of λ_φ , Y_χ decreases and hence higher value of M_{DM} is required in order to satisfy the correct relic density as depicted in above Fig.7. For simplicity we restrict our scan within the specified range of λ_φ mentioned above. However one can make the scan even for higher value of $\lambda_\varphi \gtrsim 1.0$ within the perturbativity limit. For those values of λ_φ even heavier DM mass, ($10 \text{ MeV} \lesssim M_{\text{DM}} < M_\varphi$) will be allowed by the relic density constraint.

Scenario-II: We shall now move to the second scenario where the density of φ is mainly driven by $2\varphi \rightarrow 2 \text{ SM}$ number changing process. Following our earlier discussion we know that the density of φ converts into the density of DM ($Y_\varphi(x_F^{2\varphi \rightarrow 2\text{SM}}) \simeq Y_\chi^{\text{today}}$) via the late time decay of φ . Therefore the relic density of DM given in eq.(19) becomes $\Omega_\chi h^2 \propto M_{\text{DM}} \times Y_\varphi(x_F^{2\varphi \rightarrow 2\text{SM}})$. Similar to previous scenario $Y_\varphi(x_F^{2\varphi \rightarrow 2\text{SM}})$, decreases with increase in M_{DM} in order to get fixed density and vice versa. One can also analytically express the yield of φ at freeze-out as: $Y_\varphi \propto 1/\langle\sigma v\rangle_{2\varphi \rightarrow 2\text{SM}}$ [23]. For heavier M_φ , more annihilation processes of φ to SM pairs kinematically open and enhance the cross-section. Thus $\langle\sigma v\rangle_{2\varphi \rightarrow 2\text{SM}}$ can be expressed as $\sum_{X=\text{SM}} \langle\sigma v\rangle_{\varphi\varphi \rightarrow X\bar{X}} \Theta(M_\varphi - M_X)$ where Θ is the Heaviside step function. For a fixed M_φ , Y_φ as well as Y_χ decreases as one increases $\lambda_{\varphi H}$ since $\langle\sigma v\rangle_{2\varphi \rightarrow 2\text{SM}} \propto \lambda_{\varphi H}^2$. However, here the dependence of Y_χ on M_φ is contrary to that of scenario-I. In this case with the increase in M_φ , the annihilation cross-section, $\langle\sigma v\rangle_{2\varphi \rightarrow \text{SM}}$ also increases for the aforementioned reasons and thus resulting a decrease in Y_φ as well as Y_χ [59].

Now in order to find a consistent parameter space satisfying observed relic density measured by PLANCK[6], we perform a numerical scan of the relevant parameters for scenario-II in the following range:

$$M_\varphi : \{10 - 100 \text{ GeV}\}, \quad \lambda_{\varphi H} : \{10^{-3} - 10^{-1}\}; \quad (21)$$

whereas the other parameters are kept fixed as $\mu_\varphi/M_\varphi = 0.1$, $\lambda_\varphi = 0.1$ and $y_1 = 10^{-12}$. The choices of dark sector parameters in eq.(21) ensure that $\Gamma_{2\varphi \rightarrow 2\text{SM}} \gg \Gamma_{3\varphi \rightarrow 2\varphi}$ which is required for the scenario-II. We consider M_φ up to 100 GeV, beyond that Y_φ is more

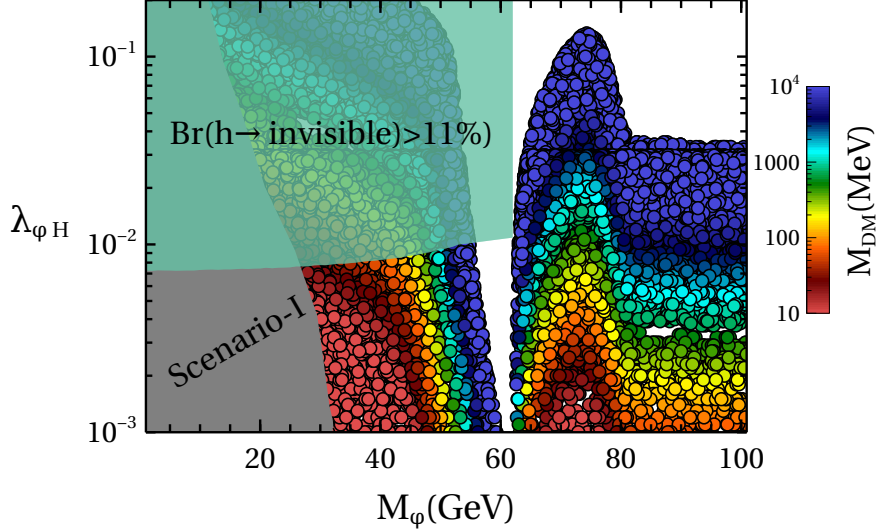


FIG. 8: *DM relic density satisfied points for scenario-II are shown in the $\lambda_{\varphi H}$ vs. M_{φ} plane with $\lambda_{\varphi} = 0.1$, $\mu_{\varphi} = 0.1M_{\varphi}$, $y_1 = 10^{-12}$ and the color gradient represents the variation in M_{DM} satisfying the correct relic density. The gray shaded region corresponds to the parameter space where scenario-I is dominating.*

suppressed resulting in a negligible contribution to ΔN_{eff} which will be discussed in due course of time.

In Fig.8 we plot correct relic density satisfied points in the M_{φ} vs. $\lambda_{\varphi H}$ plane. The variation of color gradient represents the variation of M_{DM} considered here. The correct relic density constraint sets the DM mass in the range $M_{\text{DM}}: \sim \{10 \text{ MeV} - 10 \text{ GeV}\}$ for our chosen parameters. The gray shaded region on lower left corner of the above figure represents the region where scenario-II does not work paving way to Scenario-I. With increase in $\lambda_{\varphi} (> 0.1)$, Scenario-I will start to dominate over scenario-II even with higher value of M_{φ} and the shaded region will move towards right accordingly. For $M_{\varphi} < m_h/2$, $h \rightarrow \varphi\varphi^*$ decay opens up and contributes to the SM Higgs invisible decay width ($\Gamma_h^{\text{inv.}}$) which is very precisely measured by CMS [109]. The bound from $\Gamma_h^{\text{inv.}}$ (discussed in Appendix B) excludes a significant part of the parameter space as shown by the light cyan region in Fig.8. As understood from the figure, scenario-II works in the higher range of M_{φ} and the moderate

values $\lambda_{\varphi H}$ leading to lower Y_χ as discussed earlier in this subsection. The $2\varphi \rightarrow 2\text{SM}$ annihilation cross-section near Higgs pole, $M_\varphi \sim m_h/2$, causes further suppression in Y_χ . For $M_\varphi > M_W$, more final states open up resulting in even larger $\langle\sigma v\rangle_{2\varphi\rightarrow 2\text{SM}}$. Thus to satisfy the observed DM density one has to reduce $\lambda_{\varphi H}$ in that region as shown in top right corner (white area) of the figure. Therefore the scenario-II allows higher DM mass to satisfy the correct relic density upto few GeV.

B. Contribution to ΔN_{eff} at CMB

In earlier sections, we have established that our main thrust of this whole exercise is to calculate contributions to ΔN_{eff} by extra active neutrinos produced in association with FIMP like DM from the late time decay of a self interacting dark scalar φ . Simultaneously, we have also emphasized the possibility of correlating the dark matter mass with the measured value of ΔN_{eff} . Thus, any precise determination of ΔN_{eff} would provide an indirect probe of the dynamics of dark sector involving a strongly self interacting particle φ as well as FIMP like DM. Based on our discourse in sec-IV we will now investigate dependence of dark sector model parameters in ΔN_{eff} which is completely determined by the ratio $\rho'_\nu/\rho_\nu^{\text{SM}}$.

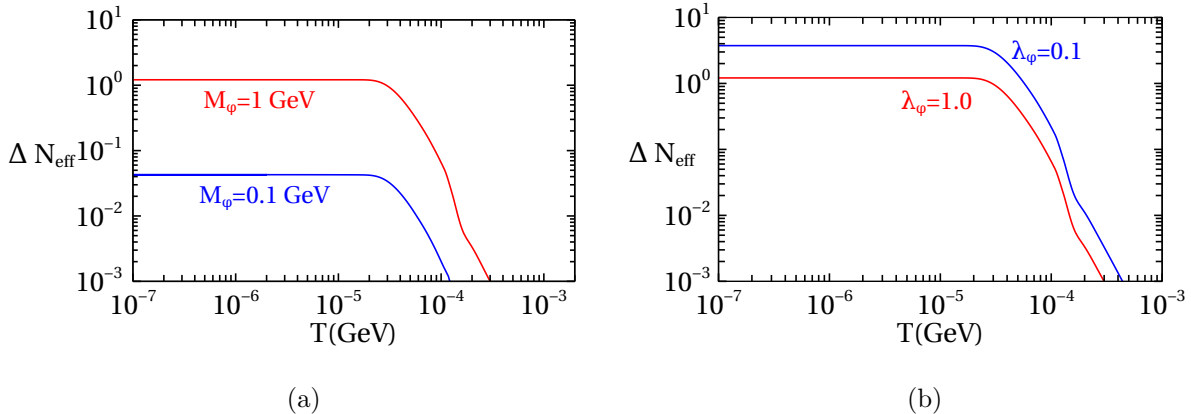


FIG. 9: Evolution of ΔN_{eff} with temperature(T) for two different values of M_φ keeping $\lambda_\varphi = 1.0$ fixed in (a) and for two different values of λ_φ keeping $M_\varphi = 1 \text{ GeV}$ fixed in (b) for scenario-I. Other parameters are kept fix as $y_1 = 10^{-12}$ and $M_{\text{DM}} = 400 \text{ keV}$.

In Fig.9 we show the evolution of ΔN_{eff} with temperature T for different set of model parameters as shown in the figure caption. We first numerically evaluate $\rho'_\nu/\rho_\nu^{\text{SM}}$ by solving eq.(19) along with eq.(11) and then plug it into eq.(16) to estimate ΔN_{eff} . From both the

figures Fig.9(a) and 9(b) we notice that at high T , the ΔN_{eff} is almost negligible because the entropy injection to neutrino bath is very small during the earlier epoch of $\varphi \rightarrow \chi\nu$ decay. With the decrease in temperature, φ freezes out from the thermal bath and decays into $\chi + \nu$ after BBN, generating a new source of active neutrinos that inject extra energy density to neutrino bath. This added neutrino density causes continuous growth of ΔN_{eff} with lowering of temperature. With further decrease in the temperature, at some point φ decay is completed and any auxiliary neutrino production also stops. Thus no more supplementary energy transfer to neutrino bath takes place and the ratio $\rho'_\nu/\rho_\nu^{\text{SM}}$ attains its maximum possible value at that temperature. After that both ρ'_ν and ρ_ν^{SM} dilutes in the same fashion with further decrease in temperature, resulting in a fixed ratio $\rho'_\nu/\rho_\nu^{\text{SM}}$ which corresponds to a constant value of ΔN_{eff} . Since $\rho'_\nu \propto Y_\varphi$ (following eq.(17)), higher value of Y_φ leads to higher energy transfer to neutrino bath resulting in larger ΔN_{eff} and vice-versa. We plot the evolution of ΔN_{eff} in Fig.9(a) for $M_\varphi = 1$ GeV (red line) and $M_\varphi = 0.1$ GeV (blue line) keeping $\lambda_\varphi = 1.0$ fixed. In Fig.9(b) we show the similar plot as in Fig.9(a) but this time for a fixed $M_\varphi = 1$ GeV and taking two values of $\lambda_\varphi = 1.0$ (red line) and 0.1 (blue line). While generating these two plots, we fix $M_{\text{DM}} = 400$ MeV, and $y_1 = 10^{-12}$. The behavior of ΔN_{eff} with the model parameters (M_φ , λ_φ and μ_φ/M_φ) is same as of Y_φ as discussed earlier for scenario-I (Fig.6(a) and 6(b)) and the same dependence is depicted in Fig.9(a) and 9(b).

The effect of $\lambda_{\varphi H}$ on ΔN_{eff} in Scenario-II is similar to Scenario-I. Following our previous argument, for any increase in the value of Higgs portal coupling $\lambda_{\varphi H}$, φ number density Y_φ decreases and that leads to a diminished contribution of active neutrinos in ΔN_{eff} . However, M_φ dependence of ΔN_{eff} shows opposite behaviour in Scenario-II than Scenario-I. Here, ΔN_{eff} decreases with an increase in M_φ . The reason for this contrary nature follows the same argument as we revealed in the context of relic density calculation. For heavier M_φ , due to enhanced phase space one gets larger $\langle\sigma v\rangle_{2\varphi\rightarrow 2\text{SM}}$ that leads to lower Y_φ and finally lower ΔN_{eff} . Hence the energy transferred to neutrino sector is too less to contribute significantly in ΔN_{eff} and the ΔN_{eff} for scenario-II will be far below the sensitivity of the current and future generation experiments. In this paper we do not display the explicit parameter dependence in ΔN_{eff} in scenario-II, however similar study could be found in [59].

Finally, we calculate the ΔN_{eff} for different values of the model parameters in scenario-I and displayed our findings in Fig.10. We present ΔN_{eff} as a function of M_φ and the color

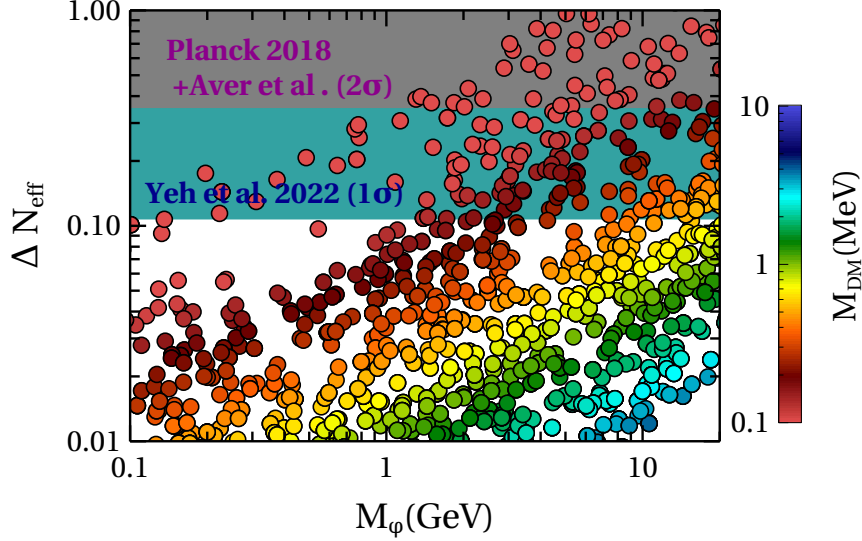


FIG. 10: Variation of ΔN_{eff} with M_φ for $\mu_\varphi/M_\varphi = 0.1$, $\lambda_{\varphi H} = 10^{-4}$ and $y_1 = 10^{-12}$ where the color gradient represents the range of DM mass in scenario-I. The current upper limits on ΔN_{eff} from Yeh et al.[78] and Planck 2018[6] combined with Aver et al.[110] are shown for comparison. Note that the cyan region below the grey band extends upto $\Delta N_{\text{eff}} = 1.00$ in this plot.

gradient represents the range of M_{DM} allowed by observed DM relic density [6]. In the figure, we show different existing exclusion bounds on ΔN_{eff} depicted by different coloured patches. We notice that a decrease in M_{DM} yields a increase in ΔN_{eff} also. This is easily understood from the fact that lower value of M_{DM} requires higher value of Y_χ to satisfy the observed relic density. As we analyzed earlier, Y_χ is governed by Y_φ and higher value of Y_χ corresponds to higher value of Y_φ . Thus for a higher value of Y_φ , more energy gets transferred to the neutrino sector, leading to the higher value of ΔN_{eff} . We also notice that higher values of M_φ corresponds to the points yielding higher value of ΔN_{eff} . This is also understandable as higher value of M_φ leads to higher value of Y_φ resulting higher value of ΔN_{eff} for the same reason discussed above. In the same plot, we present the current upper limits on ΔN_{eff} . However, it is very crucial to note that applying the Planck 2018 bound, $N_{\text{eff}} = 2.99^{+0.33}_{-0.34}$ to our case would be incorrect as that bound was derived assuming N_{eff} takes the same value during BBN ($N_{\text{eff}}^{\text{BBN}}$) and before CMB ($N_{\text{eff}}^{\text{CMB}}$). In our scenario, N_{eff} takes the standard value ($= 3.046$) during BBN and increases due to entropy injection

between BBN and CMB epoch. A recent analysis conducted by Yeh et al. [78], which aimed to investigate entropy injection between BBN and CMB epoch, pointed out an upper limit on $DN_{\text{eff}} \equiv N_{\text{eff}}^{\text{CMB}} - N_{\text{eff}}^{\text{BBN}} < 0.27$ (in 2σ limit). For our model, we translate this bound³ on $\Delta N_{\text{eff}}^{\text{CMB}}$ within 1σ by the cyan color in Fig.10 which represents the exclusion region. There also exists a BBN independent bound on ΔN_{eff} from Planck 2018 by varying both N_{eff} and Helium fraction (Y_p) which is $N_{\text{eff}} = 2.89_{-0.57}^{+0.63}$ in 2σ limit. However, combining this bound from Planck 2018 data with local measurement from Aver et al.[110], slightly improves the bound as $N_{\text{eff}} = 2.99_{-0.40}^{+0.43}$ in 2σ limit [6]. This bound is also portrayed in Fig.10, shown by the grey region that excludes ($\Delta N_{\text{eff}} \gtrsim 0.37$). Therefore, the most stringent bound applicable for our analysis is $\Delta N_{\text{eff}} \lesssim 0.11$ (in 1σ limit) [78], which excludes DM mass below a few hundred keV. The future generation experiments like SPT-3G [76] and CMB-S4 [77] may probe heavier DM mass. The allowed parameter space from the constraints of ΔN_{eff} is also consistent with bound on free streaming length of DM coming from Lyman- α forest[55, 111].

VI. CONCLUSION

In this work we have proposed a minimal extension of the Type-I seesaw model with a complex scalar singlet(φ) and a singlet Dirac fermion (χ). To ensure the stability of the lightest dark sector particle, an additional \mathcal{Z}_3 symmetry has been imposed under which φ and χ transform non-trivially while the rest of SM particles and three RHNs transform trivially.

Mass spectrum of the dark sector particles are such that the Dirac fermion χ is the lightest particle and plays the role of DM, while the singlet scalar φ is the next to lightest particle. The DM with its tiny coupling with SM bath can only be produced from the late time decay of φ and obtains its abundance. On the other hand φ remains in thermal bath due to its strong self coupling and after its freeze out it decays to DM and active neutrinos. Depending on the thermal history of φ , we have divided the analysis into two scenarios. In the first Scenario (I), φ gains its number density through freeze out mechanism via the number changing strong self-interactions within the dark sector whereas, in the second Scenario (II) φ freezes out via the SM Higgs portal coupling to SM particles. The RHNs($N_{1,2,3}$) which are

³ For our case, $\Delta N_{\text{eff}}^{\text{CMB}} \equiv DN_{\text{eff}}$ considering $N_{\text{eff}}^{\text{BBN}} = 3.046$.

responsible for generating light neutrino masses and mixing angles by type-I seesaw model, are sufficiently heavy ($M_{N_{1,2,3}} \gg T_{\text{RH}}$) such that their number densities do not contribute to DM relic. However, the presence of RHNs in the particle content allows an effective interaction between φ , χ and active neutrinos(ν) which leads to extra neutrino production from the late time decay of φ . To track the abundances of φ and χ we have solved two coupled Boltzmann equations. We have first checked the effects of different model parameters on the relic density of DM by solving those Boltzmann equations and identifying the parameter space giving correct relic density in both scenarios (I & II). Apart from producing the right amount of DM relic, the late time decay of φ makes significant impact on the total radiation energy density at the time of CMB formation which is parameterized as ΔN_{eff} . To compute ΔN_{eff} we have evaluated the extra radiation energy density injected into light neutrino bath from φ by solving the required Boltzmann equation. In scenario-I DM mass up to a few hundred keV is excluded from the present 1σ limit on ΔN_{eff} from the bound derived by Yeh et al.[78]. The future generation experiments like SPT-3G, CMB-S4 will be sensitive enough to test heavier DM mass. However, in scenario-II where the abundance of the mother particle (φ) is suppressed due to sizable interactions with SM bath, we have found that the entropy injection is insensitive to the bounds on ΔN_{eff} coming from present and future-generation experiments. Thus in this paper we have explicitly shown an alternative way of probing FIMP dark matter from the precise measurement of ΔN_{eff} even when the mother particles do not have sizable interactions with SM bath which is otherwise absent in literature. Consequently, we are expecting some very exciting results from next generation CMB experiments, like SPT-3G and CMB-S4 which can shed some light on various dark sector models, like the one discussed in this paper.

Acknowledgement

SJ and PG thanks D. Nanda for the helpful discussions during this project. The authors would like to thank Abhijit Kumar Saha, Sougata Ganguly and Deep Ghosh for useful discussion and comments. SJ is funded by CSIR, Government of India, under the NET JRF fellowship scheme with Award file No. 09/080(1172)/2020-EMR-I.

Appendix A: Theoretical constraints

Stability

The scalar potential is bounded from below when the quartic couplings of the scalar potential satisfy these co-positivity conditions[112]:

$$\lambda_H \geq 0, \quad \lambda_\varphi \geq 0, \quad \lambda_{\varphi H} + 2\sqrt{\lambda_\varphi \lambda_H} \geq 0. \quad (\text{A1})$$

The estimation of the lifetime of the desired the stable vacuum which essentially puts an upper bound on the trilinear dark coupling as [113]

$$\mu_\varphi/M_\varphi < 2\sqrt{\lambda_\varphi}. \quad (\text{A2})$$

Perturbative unitarity

The tree-level unitarity of the theory, coming from all possible $2 \rightarrow 2$ scattering amplitudes will form the S matrix and constrain the quartic couplings of the scalar potential[114]. The eigenvalues of the S matrix are bounded from above as[115]:

$$\begin{aligned} |\lambda_H| &\leq 4\pi, \quad |\lambda_{\varphi H}| \leq 8\pi, \quad |\lambda_\varphi| \leq 4\pi, \\ |2\lambda_\varphi + 3\lambda_H \pm \sqrt{2\lambda_{\varphi H}^2 + (2\lambda_\varphi - 3\lambda_H)^2}| &\leq 8\pi. \end{aligned} \quad (\text{A3})$$

The quartic and Yukawa couplings of the interaction Lagrangian should also obey following inequality equations to maintain perturbativity[116]:

$$\begin{aligned} |\lambda_H| &\lesssim \frac{2\pi}{3}, \quad |\lambda_\varphi| \lesssim \pi, \quad |\lambda_{\varphi H}| \lesssim 4\pi, \\ \text{and} \quad |y_{\varphi N}| &< \sqrt{4\pi}. \end{aligned} \quad (\text{A4})$$

Appendix B: Constraint from Higgs invisible decay

The dark complex scalar, φ is very weakly coupled with SM Higgs via the Higgs portal interaction. The late time decay of φ decides both the relic abundance of DM and the contribution to the ΔN_{eff} which require a light scalar mass of the order of MeV-few GeV which is well below $M_h/2$ (will be discussed in the next section). In that case, Higgs can

decay to the dark scalar, φ , and contribute to Higgs's invisible decay width. The Higgs invisible decay width is given by

$$\Gamma_{h \rightarrow \varphi \varphi^*} = \frac{(\lambda_{\varphi H} v)^2}{16\pi M_h} \sqrt{1 - \frac{4M_\varphi^2}{M_h^2}}, \quad (\text{B1})$$

where $M_h = 125.06$ GeV and $v = 246$ GeV. The current analysis of the CMS collaboration [109] at LHC puts a strong constraint on the Higgs invisible decay in the following form

$$\text{BR}^{\text{inv}} = \frac{\Gamma_h^{\text{inv}}}{\Gamma_h^{\text{inv}} + \Gamma_h^{\text{SM}}} < 11\% \quad , \quad (\text{B2})$$

where $\Gamma_h^{\text{SM}} = 4$ MeV. If $M_h < 2M_\varphi$ then this decay is absent. However this bound can be further improved as discussed in ref.[117]. In this work the Higgs invisible constraint only applicable for scenario-II where we require relatively large $\lambda_{\varphi H}$.

Appendix C: $3\varphi \rightarrow 2\varphi$

In our setup $3\varphi \rightarrow 2\varphi$ number changing processes in dark sector occur through $\varphi \varphi \varphi \rightarrow \varphi \varphi^*$, $\varphi \varphi^* \varphi^* \rightarrow \varphi \varphi$ and their conjugate processes i.e. $\varphi^* \varphi^* \varphi^* \rightarrow \varphi^* \varphi$, $\varphi^* \varphi^* \varphi \rightarrow \varphi^* \varphi^*$ respectively. Some of these processes are mediated by φ only and the rest are mediated by both φ and h . However, for light $M_\varphi (\lesssim \mathcal{O}(\text{GeV}))$, h-mediated diagrams are heavily suppressed due to heavy propagator suppression and small Higgs portal coupling, $\lambda_{\varphi H}$. Therefore for simplicity, one can ignore the Higgs-mediated diagrams. All the φ mediated Feynman diagrams for $\varphi \varphi \varphi \rightarrow \varphi \varphi^*$ and $\varphi \varphi^* \varphi^* \rightarrow \varphi \varphi$ processes are shown in Fig.11 and Fig.12 respectively.

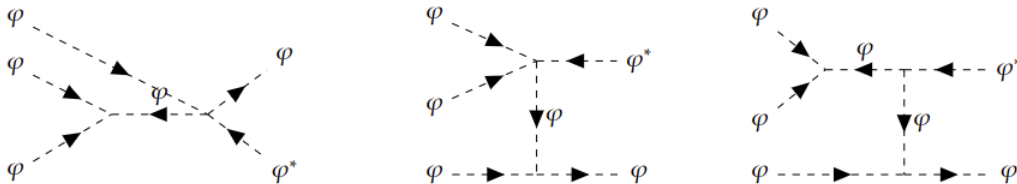


FIG. 11: Feynman diagrams for $\varphi \varphi \varphi \rightarrow \varphi \varphi^*$ number changing processes. Note that for each t -channel, there is an u -channel diagram.

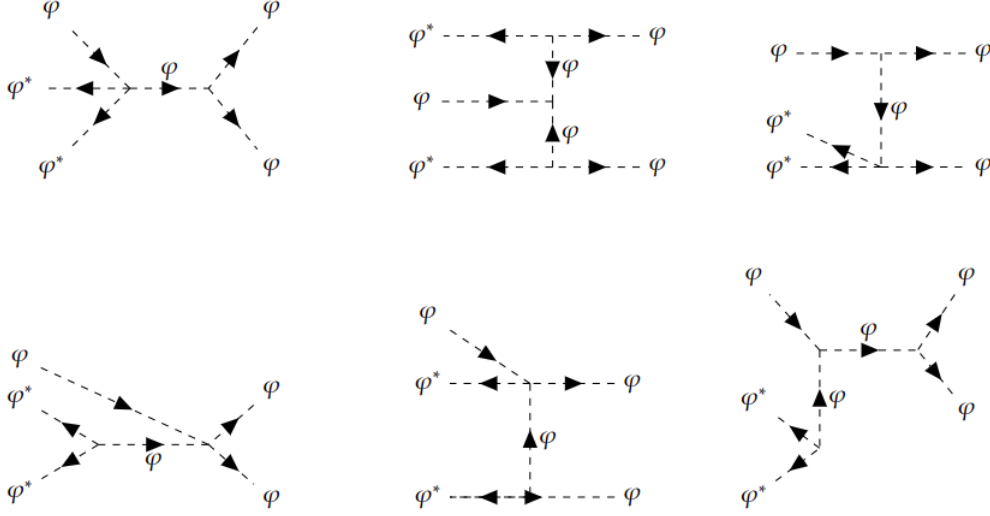


FIG. 12: Feynman diagrams for $\varphi \varphi^* \varphi^* \rightarrow \varphi \varphi$ number changing processes. Note that for each t -channel, there is an u -channel diagram.

The amplitude for $\varphi \varphi \varphi \rightarrow \varphi \varphi^*$ number changing scattering processes is given by

$$\begin{aligned}
\mathcal{M}_{\varphi\varphi\varphi\rightarrow\varphi\varphi^*} &= \mathcal{M}_1 + \mathcal{M}_2^t + \mathcal{M}_2^u + \mathcal{M}_3^t + \mathcal{M}_3^u \\
&= \left[\frac{4\mu_\varphi\lambda_\varphi}{(s-M_\varphi^2)} + \frac{4\mu_\varphi\lambda_\varphi}{(t-M_\varphi^2)} + \frac{4\mu_\varphi\lambda_\varphi}{(u-M_\varphi^2)} + \frac{\mu_\varphi^3}{(s-M_\varphi^2)(t-M_\varphi^2)} + \frac{\mu_\varphi^3}{(s-M_\varphi^2)(u-M_\varphi^2)} \right].
\end{aligned} \tag{C1}$$

And the amplitude for $\varphi \varphi^* \varphi^* \rightarrow \varphi \varphi$ number changing scattering processes is given by

$$\begin{aligned}
\mathcal{M}_{\varphi^*\varphi^*\varphi\rightarrow\varphi\varphi} &= \mathcal{M}_1 + \mathcal{M}_2^t + \mathcal{M}_2^u + \mathcal{M}_3^t + \mathcal{M}_3^u + \mathcal{M}_4 + \mathcal{M}_5^t + \mathcal{M}_5^u + \mathcal{M}_6^t + \mathcal{M}_6^u \\
&= \left[\frac{4\mu_\varphi\lambda_\varphi}{(s-M_\varphi^2)} + \frac{\mu_\varphi^3}{(t-M_\varphi^2)^2} + \frac{\mu_\varphi^3}{(u-M_\varphi^2)^2} + \frac{4\mu_\varphi\lambda_\varphi}{(t-M_\varphi^2)} + \frac{4\mu_\varphi\lambda_\varphi}{(u-M_\varphi^2)} + \frac{4\mu_\varphi\lambda_\varphi}{(s-M_\varphi^2)} \right. \\
&\quad \left. + \frac{4\mu_\varphi\lambda_\varphi}{(t-M_\varphi^2)} + \frac{4\mu_\varphi\lambda_\varphi}{(u-M_\varphi^2)} + \frac{\mu_\varphi^3}{(t-M_\varphi^2)(s-M_\varphi^2)} + \frac{\mu_\varphi^3}{(u-M_\varphi^2)(s-M_\varphi^2)} \right].
\end{aligned} \tag{C2}$$

The total thermal averaged cross section for $3\varphi \rightarrow 2\varphi$ number changing processes can be

expressed using non-relativistic approximation as[118]:

$$\begin{aligned}
\langle \sigma v^2 \rangle_{3\varphi \rightarrow 2\varphi} &= \langle \sigma v^2 \rangle_{\varphi\varphi\varphi \rightarrow \varphi\varphi^*} + \langle \sigma v^2 \rangle_{\varphi\varphi^*\varphi^* \rightarrow \varphi\varphi} \\
&\approx \frac{\sqrt{5}}{192\pi M_\varphi^3} \left(|\mathcal{M}_{\varphi\varphi\varphi \rightarrow \varphi\varphi^*}|^2 + |\mathcal{M}_{\varphi\varphi^*\varphi^* \rightarrow \varphi\varphi}|^2 \right) \\
&\quad + \frac{\sqrt{5}}{192\pi M_\varphi^3} \left(|\mathcal{M}_{\varphi\varphi^*\varphi^* \rightarrow \varphi\varphi}|^2 + |\mathcal{M}_{\varphi\varphi^*\varphi \rightarrow \varphi^*\varphi^*}|^2 \right) \\
&= \frac{\sqrt{5}}{192\pi M_\varphi^3} \left(2|\mathcal{M}_{\varphi\varphi\varphi \rightarrow \varphi\varphi^*}|^2 + 2|\mathcal{M}_{\varphi\varphi^*\varphi^* \rightarrow \varphi\varphi}|^2 \right), \tag{C3}
\end{aligned}$$

where $|\mathcal{M}_{\varphi\varphi\varphi \rightarrow \varphi\varphi^*}|^2 = |\mathcal{M}_{\varphi\varphi^*\varphi^* \rightarrow \varphi\varphi}|^2$ and $|\mathcal{M}_{\varphi\varphi^*\varphi \rightarrow \varphi^*\varphi^*}|^2 = |\mathcal{M}_{\varphi\varphi^*\varphi^* \rightarrow \varphi\varphi}|^2$.

Appendix D: $2\varphi \rightarrow 2$ SM and φ SM $\rightarrow \varphi$ SM

There is another type of number-changing process between the dark sector, φ , and the visible sector, SM where two dark scalar φ annihilates into two SM particles via h mediated diagram. Note that our analysis mostly focuses on the light-dark scalar with mass up to a few GeV. Therefore φ can only annihilate into light fermion pairs. The Feynman diagrams of corresponding number-changing processes are shown in Fig.13.

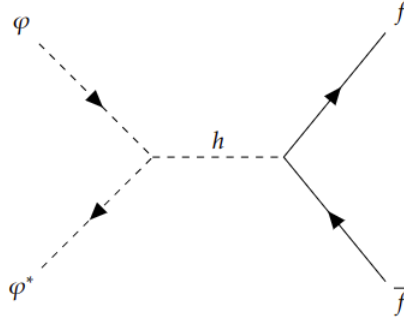


FIG. 13: Feynman Diagrams for $\varphi \varphi^* \rightarrow f\bar{f}$ where f stands for SM fermions excluding top quark.

The thermal averaged cross-section for $2\varphi \rightarrow 2$ SM number changing process is given by:

$$\begin{aligned}
\langle \sigma v \rangle_{2\varphi \rightarrow 2\text{SM}} &= \sum_f \langle \sigma v \rangle_{\varphi\varphi^* \rightarrow f\bar{f}} \\
&= \sum_f \frac{x}{16TM_\varphi^4 K_2(x)^2} \int_{4M_\varphi^2}^{\infty} (\sigma v)_{\varphi\varphi^* \rightarrow f\bar{f}} K_1\left(\frac{\sqrt{s}}{T}\right) s \sqrt{s - 4M_\varphi^2} ds \tag{D1}
\end{aligned}$$

where $x = \frac{M_\varphi}{T}$ and $(\sigma v)_{\varphi\varphi^* \rightarrow f\bar{f}}$ can be written as:

$$(\sigma v)_{\varphi\varphi \rightarrow f\bar{f}} = \left(\frac{1}{4\pi s\sqrt{s}} \frac{N_c \lambda_\varphi^2 m_f^2}{(s - m_h^2)^2 + m_h^2 \Gamma_h^2} (s - 4m_f^2)^{\frac{3}{2}} \right) \Theta(M_\varphi - m_f). \quad (\text{D2})$$

In the above expression $N_c = 1$ for leptons and $N_c = 3$ for quarks. However for scenario-II we considered M_φ upto 100 GeV where interactions having Higgs mediated gauge boson final states are contributing to $2\varphi \rightarrow 2\text{SM}$ processes.

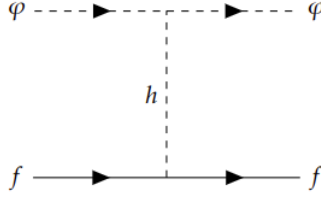


FIG. 14: Feynman Diagrams for $\varphi f \rightarrow \varphi f$ where f stands for SM fermion excluding top quark.

The scattering between DM and SM, $\varphi f \rightarrow \varphi f$ is also important for our discussion which is required for analysing the kinetic equilibrium of the DM in early universe. The Feynman diagram for the scattering between DM and SM fermions are shown in Fig.14.

The thermal averaged scattering cross-section between DM and SM is followed by:

$$\begin{aligned} \langle \sigma v \rangle_{\varphi f \rightarrow \varphi f} &= \sum_f \left(\langle \sigma v \rangle_{\varphi f \rightarrow \varphi f} + \langle \sigma v \rangle_{\varphi^* f \rightarrow \varphi^* f} \right) = 2 \sum_f \langle \sigma v \rangle_{\varphi f \rightarrow \varphi f} \\ &= \sum_f \frac{x}{16TM_\varphi^2 m_f^2 K_2(M_\varphi/T) K_2(m_f/T)} \\ &\quad \times \int_{(M_\varphi + m_f)^2}^{\infty} (\sigma v)_{\varphi f \rightarrow \varphi f} K_1\left(\frac{\sqrt{s}}{T}\right) s \sqrt{s - (M_\varphi + m_f)^2} ds, \quad (\text{D3}) \end{aligned}$$

where $x = \frac{M_\varphi}{T}$ and the scattering cross-section, $(\sigma v)_{\varphi f \rightarrow \varphi f}$ is given by,

$$\begin{aligned} (\sigma v)_{\varphi f \rightarrow \varphi f} &= \frac{1}{4\pi s\sqrt{s}} \frac{1}{2\sqrt{s}} \sqrt{[s - (M_\varphi + m_f)^2][s - (M_\varphi - m_f)^2]} \\ &\quad \times \left[-2(t - 4M_\varphi^2) \left(\frac{\lambda_\varphi H v}{t - m_h^2} \right)^2 \right]. \quad (\text{D4}) \end{aligned}$$

Appendix E: Condition for Kinetic equilibrium

Following the discussion in sec.III the Kinetic equilibrium is ensured by the following inequality,

$$\Gamma_{[\varphi f \rightarrow \varphi f]}(T) \gtrsim \mathcal{H}(T). \quad (\text{E1})$$

As shown in Fig.14 φ undergoes elastic scattering processes with SM fermions. The interaction rate is given by,

$$\Gamma_{[\varphi f \rightarrow \varphi f]}(T) = n_f^{eq}(T) \langle \sigma v \rangle_{\varphi f \rightarrow \varphi f}, \quad (\text{E2})$$

where, $n_f^{eq}(T)$ is the equilibrium number densities of fermions and given by,

$$n_f^{eq}(T) = \frac{g_f}{(2\pi)^{3/2}} 4\pi m_f^2 T K_2\left(\frac{m_f}{T}\right) \quad (\text{E3})$$

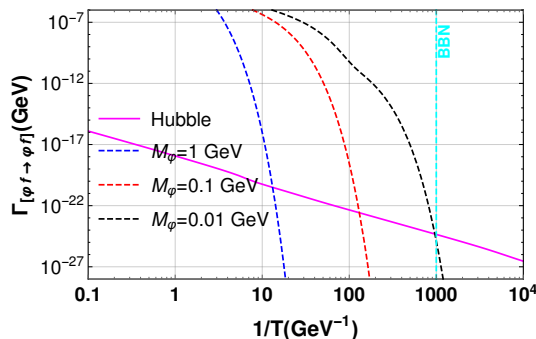


FIG. 15: Evolution of $\Gamma_{[\varphi f \rightarrow \varphi f]}$ with $1/T$ keeping $\lambda_{\varphi H} = 10^{-4}$, $\mu_{\varphi}/M_{\varphi} = 0.1$ for three different mass of φ , $M_{\varphi} = 1, 0.1, 0.01$ GeV depicted by blue, red and black dashed line respectively. The solid magenta line signifies $\mathcal{H}(T)$.

In Fig.15 we display the evolution of elastic scattering rate $\Gamma_{[\varphi f \rightarrow \varphi f]}$ with $1/T$ for different values of $M_{\varphi} = 1, 0.1, 0.01$ GeV depicted by blue, red and black dashed line respectively. In the same plot we display the expansion rate \mathcal{H} for comparison, shown by the solid magenta line. We notice that the condition for kinetic equilibrium doesn't hold after $T < M_{\varphi}/10$. In this work we took the lowest value of $M_{\varphi} = 0.1$ GeV and the kinetic equilibrium breaks long before BBN ($T \sim 1$ MeV). Note that the kinetic equilibrium can be possible even after BBN for $M_{\varphi} \lesssim 0.01$ GeV which can give rise to observable imprints [79, 119]. For example ref.[79] has shown that if particle with $\mathcal{O}(\text{MeV})$ mass remains in thermal equilibrium with neutrino bath after neutrino decoupling leads to increment in N_{eff} . However, to avoid such complications, we restrict the parameter space in our work with lowest mass of φ as 0.1 GeV such that the kinetic decoupling happens long before BBN ($T \sim 1$ MeV).

[1] S. Chatrchyan et al. (CMS), Phys. Lett. B **716**, 30 (2012), 1207.7235.

- [2] G. Aad et al. (ATLAS), *Phys. Lett. B* **716**, 1 (2012), 1207.7214.
- [3] F. Zwicky, *Helv. Phys. Acta* **6**, 110 (1933).
- [4] V. C. Rubin and W. K. Ford, Jr., *Astrophys. J.* **159**, 379 (1970).
- [5] D. Clowe, M. Bradac, A. H. Gonzalez, M. Markevitch, S. W. Randall, C. Jones, and D. Zaritsky, *Astrophys. J. Lett.* **648**, L109 (2006), astro-ph/0608407.
- [6] N. Aghanim et al. (Planck), *Astron. Astrophys.* **641**, A6 (2020), [Erratum: *Astron. Astrophys.* 652, C4 (2021)], 1807.06209.
- [7] K. Abe et al. (T2K), *Phys. Rev. Lett.* **107**, 041801 (2011), 1106.2822.
- [8] Y. Abe et al. (Double Chooz), *Phys. Rev. Lett.* **108**, 131801 (2012), 1112.6353.
- [9] F. P. An et al. (Daya Bay), *Phys. Rev. Lett.* **108**, 171803 (2012), 1203.1669.
- [10] J. K. Ahn et al. (RENO), *Phys. Rev. Lett.* **108**, 191802 (2012), 1204.0626.
- [11] P. Adamson et al. (MINOS), *Phys. Rev. Lett.* **110**, 171801 (2013), 1301.4581.
- [12] P. A. Zyla et al. (Particle Data Group), *PTEP* **2020**, 083C01 (2020).
- [13] P. Minkowski, *Phys. Lett. B* **67**, 421 (1977).
- [14] R. N. Mohapatra and G. Senjanovic, *Phys. Rev. Lett.* **44**, 912 (1980).
- [15] J. Schechter and J. W. F. Valle, *Phys. Rev. D* **22**, 2227 (1980).
- [16] M. Gell-Mann, P. Ramond, and R. Slansky, *Conf. Proc. C* **790927**, 315 (1979), 1306.4669.
- [17] R. N. Mohapatra and G. Senjanovic, *Phys. Rev. D* **23**, 165 (1981).
- [18] G. Lazarides, Q. Shafi, and C. Wetterich, *Nucl. Phys. B* **181**, 287 (1981).
- [19] C. Wetterich, *Nucl. Phys. B* **187**, 343 (1981).
- [20] J. Schechter and J. W. F. Valle, *Phys. Rev. D* **25**, 774 (1982).
- [21] B. Brahmachari and R. N. Mohapatra, *Phys. Rev. D* **58**, 015001 (1998), hep-ph/9710371.
- [22] R. Foot, H. Lew, X. G. He, and G. C. Joshi, *Z. Phys. C* **44**, 441 (1989).
- [23] E. W. Kolb and M. S. Turner, *The Early Universe*, vol. 69 (1990), ISBN 978-0-201-62674-2.
- [24] J. L. Feng, *Ann. Rev. Astron. Astrophys.* **48**, 495 (2010), 1003.0904.
- [25] L. Roszkowski, E. M. Sessolo, and S. Trojanowski, *Rept. Prog. Phys.* **81**, 066201 (2018), 1707.06277.
- [26] M. Schumann, *J. Phys. G* **46**, 103003 (2019), 1903.03026.
- [27] T. Lin, *PoS* **333**, 009 (2019), 1904.07915.
- [28] G. Arcadi, M. Dutra, P. Ghosh, M. Lindner, Y. Mambrini, M. Pierre, S. Profumo, and F. S. Queiroz, *Eur. Phys. J. C* **78**, 203 (2018), 1703.07364.

- [29] A. Tan et al. (PandaX-II), Phys. Rev. Lett. **117**, 121303 (2016), 1607.07400.
- [30] E. Aprile et al. (XENON), Phys. Rev. Lett. **119**, 181301 (2017), 1705.06655.
- [31] D. S. Akerib et al. (LUX), Phys. Rev. Lett. **118**, 021303 (2017), 1608.07648.
- [32] C. Amole et al. (PICO), Phys. Rev. D **100**, 022001 (2019), 1902.04031.
- [33] M. Aguilar et al. (AMS), Phys. Rev. Lett. **110**, 141102 (2013).
- [34] J. Buckley et al., in Community Summer Study 2013: Snowmass on the Mississippi (2013), 1310.7040.
- [35] J. M. Gaskins, Contemp. Phys. **57**, 496 (2016), 1604.00014.
- [36] A. Albert et al. (Fermi-LAT, DES), Astrophys. J. **834**, 110 (2017), 1611.03184.
- [37] M. L. Ahnen et al. (MAGIC, Fermi-LAT), JCAP **02**, 039 (2016), 1601.06590.
- [38] T. Bringmann and C. Weniger, Phys. Dark Univ. **1**, 194 (2012), 1208.5481.
- [39] M. Cirelli, PoS **ICRC2015**, 014 (2016), 1511.02031.
- [40] F. Kahlhoefer, Int. J. Mod. Phys. A **32**, 1730006 (2017), 1702.02430.
- [41] A. Boveia and C. Doglioni, Ann. Rev. Nucl. Part. Sci. **68**, 429 (2018), 1810.12238.
- [42] L. J. Hall, K. Jedamzik, J. March-Russell, and S. M. West, JHEP **03**, 080 (2010), 0911.1120.
- [43] J. König, A. Merle, and M. Totzauer, JCAP **11**, 038 (2016), 1609.01289.
- [44] A. Biswas and A. Gupta, JCAP **09**, 044 (2016), [Addendum: JCAP 05, A01 (2017)], 1607.01469.
- [45] A. Biswas and A. Gupta, JCAP **03**, 033 (2017), [Addendum: JCAP 05, A02 (2017)], 1612.02793.
- [46] N. Bernal, M. Heikinheimo, T. Tenkanen, K. Tuominen, and V. Vaskonen, Int. J. Mod. Phys. A **32**, 1730023 (2017), 1706.07442.
- [47] D. Borah, B. Karmakar, and D. Nanda, JCAP **07**, 039 (2018), 1805.11115.
- [48] G. Elor, R. McGehee, and A. Pierce, Phys. Rev. Lett. **130**, 031803 (2023), 2112.03920.
- [49] P. N. Bhattiprolu, G. Elor, R. McGehee, and A. Pierce, JHEP **01**, 128 (2023), 2210.15653.
- [50] J. Heeck and D. Teresi, Phys. Rev. D **96**, 035018 (2017), 1706.09909.
- [51] K. J. Bae, A. Kamada, S. P. Liew, and K. Yanagi, JCAP **01**, 054 (2018), 1707.06418.
- [52] S. Boulebnane, J. Heeck, A. Nguyen, and D. Teresi, JCAP **04**, 006 (2018), 1709.07283.
- [53] G. Ballesteros, M. A. G. Garcia, and M. Pierre, JCAP **03**, 101 (2021), 2011.13458.
- [54] F. D’Eramo and A. Lenoci, JCAP **10**, 045 (2021), 2012.01446.
- [55] Q. Decant, J. Heisig, D. C. Hooper, and L. Lopez-Honorez, JCAP **03**, 041 (2022), 2111.09321.

- [56] S.-P. Li, X.-Q. Li, X.-S. Yan, and Y.-D. Yang, *Phys. Rev. D* **104**, 115007 (2021), 2106.07122.
- [57] Y. Cheng and W. Liao, *Phys. Lett. B* **815**, 136118 (2021), 2012.01875.
- [58] X. Chu, T. Hambye, and M. H. G. Tytgat, *JCAP* **05**, 034 (2012), 1112.0493.
- [59] D. K. Ghosh, S. Jeusun, and D. Nanda (2022), 2206.04940.
- [60] T. Hambye, M. H. G. Tytgat, J. Vandecasteele, and L. Vanderheyden, *Phys. Rev. D* **100**, 095018 (2019), 1908.09864.
- [61] Y. Hochberg, E. Kuflik, T. Volansky, and J. G. Wacker, *Phys. Rev. Lett.* **113**, 171301 (2014), 1402.5143.
- [62] Y. Hochberg, E. Kuflik, H. Murayama, T. Volansky, and J. G. Wacker, *Phys. Rev. Lett.* **115**, 021301 (2015), 1411.3727.
- [63] S. Bhattacharya, P. Ghosh, and S. Verma, *JCAP* **01**, 040 (2020), 1904.07562.
- [64] S. W. Randall, M. Markevitch, D. Clowe, A. H. Gonzalez, and M. Bradac, *Astrophys. J.* **679**, 1173 (2008), 0704.0261.
- [65] W. J. G. de Blok, *Adv. Astron.* **2010**, 789293 (2010), 0910.3538.
- [66] M. Boylan-Kolchin, J. S. Bullock, and M. Kaplinghat, *Mon. Not. Roy. Astron. Soc.* **415**, L40 (2011), 1103.0007.
- [67] N. Bernal, C. Cosme, and T. Tenkanen, *Eur. Phys. J. C* **79**, 99 (2019), 1803.08064.
- [68] N. Bernal, X. Chu, C. Garcia-Cely, T. Hambye, and B. Zaldivar, *JCAP* **03**, 018 (2016), 1510.08063.
- [69] P. Ghosh, P. Konar, A. K. Saha, and S. Show, *JCAP* **10**, 017 (2022), 2112.09057.
- [70] R. R. Khuri, *Mod. Phys. Lett. A* **13**, 1407 (1998), gr-qc/9803095.
- [71] S. Riemer-Sorensen, D. Parkinson, and T. M. Davis, *Publ. Astron. Soc. Austral.* **30**, e029 (2013), 1301.7102.
- [72] G. Mangano, G. Miele, S. Pastor, T. Pinto, O. Pisanti, and P. D. Serpico, *Nucl. Phys. B* **729**, 221 (2005), hep-ph/0506164.
- [73] E. Grohs, G. M. Fuller, C. T. Kishimoto, M. W. Paris, and A. Vlasenko, *Phys. Rev. D* **93**, 083522 (2016), 1512.02205.
- [74] P. F. de Salas and S. Pastor, *JCAP* **07**, 051 (2016), 1606.06986.
- [75] K. Akita and M. Yamaguchi, *JCAP* **08**, 012 (2020), 2005.07047.
- [76] J. S. Avva et al. (SPT-3G), *J. Phys. Conf. Ser.* **1468**, 012008 (2020), 1911.08047.
- [77] K. N. Abazajian et al. (CMB-S4) (2016), 1610.02743.

- [78] T.-H. Yeh, J. Shelton, K. A. Olive, and B. D. Fields, *JCAP* **10**, 046 (2022), 2207.13133.
- [79] C. Boehm, M. J. Dolan, and C. McCabe, *JCAP* **12**, 027 (2012), 1207.0497.
- [80] C. Brust, D. E. Kaplan, and M. T. Walters, *JHEP* **12**, 058 (2013), 1303.5379.
- [81] K. M. Nollett and G. Steigman, *Phys. Rev. D* **91**, 083505 (2015), 1411.6005.
- [82] K. N. Abazajian and J. Heeck, *Phys. Rev. D* **100**, 075027 (2019), 1908.03286.
- [83] D. Borah, S. Mahapatra, D. Nanda, and N. Sahu, *Phys. Lett. B* **833**, 137297 (2022), 2204.08266.
- [84] A. Biswas, D. K. Ghosh, and D. Nanda, *JCAP* **10**, 006 (2022), 2206.13710.
- [85] S. Knapen, T. Lin, and K. M. Zurek, *Phys. Rev. D* **96**, 115021 (2017), 1709.07882.
- [86] D. Choudhury and D. Sachdeva, *Phys. Rev. D* **100**, 075007 (2019), 1906.06364.
- [87] A. Biswas, D. Borah, N. Das, and D. Nanda (2022), 2205.01144.
- [88] S. Ganguly, S. Roy, and A. K. Saha (2022), 2201.00854.
- [89] S. Vagnozzi, *Phys. Rev. D* **102**, 023518 (2020), 1907.07569.
- [90] A. S. de Jesus, N. Pinto-Neto, F. S. Queiroz, J. Silk, and D. R. da Silva, *Eur. Phys. J. C* **83**, 203 (2023), 2212.13272.
- [91] A. Ibarra, E. Molinaro, and S. T. Petcov, *JHEP* **09**, 108 (2010), 1007.2378.
- [92] M. Farina, D. Pappadopulo, J. T. Ruderman, and G. Trevisan, *JHEP* **12**, 039 (2016), 1607.03108.
- [93] D. Pappadopulo, J. T. Ruderman, and G. Trevisan, *Phys. Rev. D* **94**, 035005 (2016), 1602.04219.
- [94] R. J. Scherrer and M. S. Turner, *Astrophys. J.* **331**, 19 (1988).
- [95] D. Hooper, F. S. Queiroz, and N. Y. Gnedin, *Phys. Rev. D* **85**, 063513 (2012), 1111.6599.
- [96] W. Fischler and J. Meyers, *Phys. Rev. D* **83**, 063520 (2011), 1011.3501.
- [97] J. L. Menestrina and R. J. Scherrer, *Phys. Rev. D* **85**, 047301 (2012), 1111.0605.
- [98] J. Hasenkamp and J. Kersten, *JCAP* **08**, 024 (2013), 1212.4160.
- [99] A. C. Sobotka, A. L. Erickcek, and T. L. Smith, *Phys. Rev. D* **107**, 023525 (2023), 2207.14308.
- [100] J. Kersten and A. Y. Smirnov, *Phys. Rev. D* **76**, 073005 (2007), 0705.3221.
- [101] S. Hannestad, *Phys. Rev. D* **70**, 043506 (2004), astro-ph/0403291.
- [102] S. Davidson, M. Losada, and A. Riotto, *Phys. Rev. Lett.* **84**, 4284 (2000), hep-ph/0001301.
- [103] J. Jaeckel and W. Yin, *Phys. Rev. D* **107**, 015001 (2023), 2206.06376.
- [104] K. Nakayama, S. Saito, Y. Suwa, and J. Yokoyama, *JCAP* **06**, 020 (2008), 0804.1827.

- [105] D. G. Figueroa and E. H. Tanin, *JCAP* **08**, 011 (2019), 1905.11960.
- [106] M. Artymowski, O. Czerwinska, Z. Lalak, and M. Lewicki, *JCAP* **04**, 046 (2018), 1711.08473.
- [107] A. Biswas, D. Borah, and D. Nanda, *JCAP* **09**, 014 (2018), 1806.01876.
- [108] R. Coy, A. Gupta, and T. Hambye, *Phys. Rev. D* **104**, 083024 (2021), 2104.00042.
- [109] A. M. Sirunyan et al. (CMS), *Phys. Lett. B* **793**, 520 (2019), 1809.05937.
- [110] E. Aver, K. A. Olive, and E. D. Skillman, *JCAP* **07**, 011 (2015), 1503.08146.
- [111] A. Boyarsky, J. Lesgourgues, O. Ruchayskiy, and M. Viel, *JCAP* **05**, 012 (2009), 0812.0010.
- [112] K. Kannike, *Eur. Phys. J. C* **72**, 2093 (2012), 1205.3781.
- [113] A. Hektor, A. Hryczuk, and K. Kannike, *JHEP* **03**, 204 (2019), 1901.08074.
- [114] J. Horejsi and M. Kladiva, *Eur. Phys. J. C* **46**, 81 (2006), hep-ph/0510154.
- [115] S. Bhattacharya, P. Ghosh, T. N. Maity, and T. S. Ray, *JHEP* **10**, 088 (2017), 1706.04699.
- [116] R. N. Lerner and J. McDonald, *Phys. Rev. D* **80**, 123507 (2009), 0909.0520.
- [117] T. Biekötter and M. Pierre, *Eur. Phys. J. C* **82**, 1026 (2022), 2208.05505.
- [118] M. M. Pierre, Ph.D. thesis, U. Paris-Saclay (2018), 1901.05822.
- [119] C. M. Ho and R. J. Scherrer, *Phys. Rev. D* **87**, 023505 (2013), 1208.4347.